

Modelling and industrial application of flow through two-dimensional porous media

by

J.P. du Plessis



Thesis presented in partial fulfilment of the requirements for the degree of
Master of Engineering Science at the University of Stellenbosch.

Promoter: Dr. G.J.F. Smit

March 2002

Declaration

I, the undersigned, hereby declare that the work contained in this thesis is my own original work and that I have not previously in its entirety or in part submitted it at any university for a degree.

Abstract

A Representative Unit Cell (RUC) model for flow through two-dimensional porous media is presented and applied to two industrial related problems. The first application is to that of cross-flow in tube banks. Both staggered and square (inline) configurations are investigated and the model results are compared to experimental data. The second application is to flow through a stack in a timber-drying kiln. The RUC model is applied to the anisotropic timber stack ends and the centre part is modelled with a standard duct flow solution. The results of the models applied to a timber stack are compared to experimental data obtained from model tests undertaken in a wind tunnel. The results of the RUC and duct flow models are found to be in excellent agreement with the data of the experimental models. These models may be used to optimize kiln designs.

Opsomming

'n Verteenwoordigende Eenheid Sel (VES) model vir vloeï deur twee-dimensionele poreuse media word weergegee en toegepas op twee industriële toepassings. Die eerste toepassing is op dwarsvloeï deur banke van buise. Beide gestapelde en inlyn konfigurasies word ondersoek waarvan die model resulte met eksperimentele data vergelyk word. Die tweede toepassing is op vloeï deur 'n stapel in 'n hout-droogoond. Die VES model word toegepas op die anisotropiese ente van houtstapels en die middelste seksie word gemodelleer deur 'n standaard kanaalvloeï oplossing. Die resultate van die modelle toegepas op n 'houtstapel word vergelyk met eksperimentele data verkry uit model toetse wat in 'n wind-tonnel uitgevoer is. Die VES en kanaalvloeï modelle se resultate stem uitstekend ooreen met die data van die eksperimentele modelle. Hierdie modelle kan gebruik word om die ontwerp van droogoonde te optimeer.

Contents

Abstract	i
Opsomming	ii
List of Figures	vi
List of Tables	ix
Nomenclature	x
1 Introduction	1
1.1 Historical Overview	2
1.2 Classification	5
1.3 Porous Media Modelling Parameters	6
1.4 Two-dimensional Porous Media	8
2 Volumetric Averaging with a REV	10
2.1 Representative Elementary Volume	10
2.2 Slattery's Averaging Theorem	13

2.3	Time Derivative	14
3	Averaging of Transport Equations	16
3.1	Volume Averaged Variables	16
3.2	Conservation of Mass	17
3.3	Momentum Transport Equation	18
3.4	Interstitial Streamwise Transport	21
3.5	Lineality and Tortuosity	22
4	Closure Modelling With a RUC	24
4.1	A RUC for Anisotropic Fibres	24
4.2	Closure	27
4.3	Asymptote Matching	32
4.4	Friction Factor and Reynolds Number	33
5	Cross-flow in Tube Banks	36
5.1	Cross-flow Forces on a Tube in a Bank	38
5.2	Pressure Loss Across a Bank of Tubes	42
5.3	Tube Bank Modelled with a RUC	49
5.4	Comparison of Experimental Data with Results of the RUC Model	52
6	Flow Through a Stack in a Timber-drying Kiln	57

6.1	Modelling of the Stack Centre	61
6.2	Modelling of the Stack Ends	65
6.3	Experimental Analysis of the Stack Centre	67
6.4	Experimental Analysis of the Stack Ends	70
6.5	Comparison of Results	72
7	Conclusions and Recommendations	77
A	Slattery's Averaging Theorem	80
B	Plane Poiseuille Flow	83
	Bibliography	85

List of Figures

2.1	Representative Elementary Volume (REV).	11
3.1	Representative Elementary Volume (REV).	21
4.1	RUC for a two-dimensional anisotropic fibre bed.	25
4.2	Streamlines in a two-dimensional anisotropic RUC for the Darcy flow range.	28
4.3	Interstitial laminar flow with recirculation for a two-dimensional RUC (not an exact solution).	29
4.4	Two-dimensional anisotropic RUC for the Forchheimer flow range.	30
5.1	Illustration of a staggered array with the area inside the dashed line, showing the size of the smallest periodic volume.	37
5.2	Illustration of a square array with the area inside the dashed line, showing the size of the smallest periodic volume.	37
5.3	The point of impact on a cylinder in a square array tube bank as determined from the experimental data of Zukauskas and Ulinskas, 1983.	40

5.4 Drag coefficient on a smooth tube in a bank as by Equation sets 5.9 and 5.10 with $a = b = 2$. For convenience, the drag coefficient of a single cylinder in the free stream is given and is comparable with the other drag coefficient given when V_{max} at a tube in a bank is assumed to be the equivalent of q around a cylinder in a free stream. C_D is based on the tube frontal area, $A_{\perp} = DL$. Note that the characteristic speed on which the Re number is based, is different between plots as evident from expressions associated with each. 42

5.5 Pressure drop across a staggered tube bank. Equations 5.13 to 5.21 and the RUC model (Equation 5.35) results are displayed. 47

5.6 Pressure drop across a square tube bank. Equations 5.22 to 5.28 and the RUC model (Equation 5.35) results are displayed. 49

5.7 The two terms of Equation 5.35 are used to illustrate the difference between using a constant drag coefficient and one that is based on the Reynolds number. $C_D \approx 1.1$ for $Re_{qD} = 1000$ and $C_D = f(Re_{qD})$ is obtained from Equation 5.36. 52

5.8 The porous media friction factor for a staggered tube bank. Experimental results of Zukauskas and Ulinskas, 1983, are compared with the RUC model (Equation 5.35). 54

5.9 The porous media friction factor for a square array tube bank. Experimental results of Zukauskas and Ulinskas, 1983, are compared with the RUC model (Equation 5.35). 55

6.1 A section through a typical timber-drying kiln a with stack in the centre. . . 58

6.2 Top view of a typical layer in a cross-piled stack showing stickers channelling the airflow in the streamwise direction. The board layers above and under the one shown is a mirror image of the displayed layer. Compare this with Figure 6.3 for clarity. 59

6.3	A picture of a typical cross-piled timber stack to be dried in a kiln. Note the spacing of the stickers of which the ends are visible on the left. Picture taken at Mondi Timbers, Stellenbosch.	60
6.4	Illustration of streamlines in the region of sudden contraction between boards when the flow enters a stack.	63
6.5	A view of a section through the stack end perpendicular to the streamwise direction with the area inside the dashed line, showing the size of the smallest periodic volume.	66
6.6	Picture of an experimental stack in a wind-tunnel. Model of central part seen from tunnel inlet.	68
6.7	Test model of stack end with the streamwise direction from left to right. . .	71
6.8	The comparison of the three mathematical solutions in Chapter 4 and the experimental data from the stack end model.	73
6.9	Pressure loss across the experimental stacks as tested in the wind tunnel compared with mathematical models.	74
A.1	Translation of a REV along an arbitrary curve s	81
B.1	Plane Poiseuille flow between stationary parallel plates.	84

List of Tables

6.1	C_D for 2-D rectangular bodies at $Re_{qL_{\perp}} \geq 10^4$ from White, 1994.	66
6.2	Dimensional values of experimental stack resembling the centre of a real stack.	67
6.3	Air properties present during experiment.	69
6.4	Experimental data obtained from the stack centre model in the wind tunnel.	69
6.5	Dimensional values as used in the RUC of the experimental stack to model the staggered ends of a real stack.	70
6.6	Air properties present during experiments.	70
6.7	Experimental data obtained from the model of a stack end in the wind tunnel.	72
6.8	Values used to produce results for the RUC solution plotted in Figure 6.8.	74
6.9	Values used for the stack centre models of duct flow and Idelchik, 1986, which are plotted in Figure 6.9. Note the difference between ε (surface roughness) and ϵ (porosity).	75
6.10	Example of how Figure 6.9 can be interpreted.	76

Nomenclature

Standard Characters

a, b	[]	Dimension ratio in tube bank
A, B	[]	Darcy and Forchheimer coefficients respectively
A	[m^2]	Characteristic area
AR	[]	Aspect ratio
c	[]	Constant
c_f	[]	Skin friction coefficient
C	[m]	Stack depth in streamwise direction
C_D	[]	Drag coefficient
d_h	[m]	Duct hydraulic diameter
d	[m]	Linear RUC dimension
D	[m]	Tube/cylinder diameter, duct height
D	[m]	Characteristic dimension of porous medium
Eu	[]	Euler number
f	[]	Fanning friction factor
f_D	[]	Darcy friction factor, also Darcy-Weisbach friction factor
F	[m^{-2}]	Friction factor for porous media, $F = \epsilon/K$
\mathcal{F}	[N]	Force
g	[m/s^2]	Gravitational acceleration, $g \approx 9.81$
h	[m]	Head loss
\mathcal{I}	[]	Variable used to represent integral term
k	[]	Number of tube rows in streamwise direction
K	[]	Darcy permeability coefficient

Standard Characters ...continued

L	[m]	Length
l	[m]	Linear dimension
\mathcal{L}	[]	Lineality
n	[]	Constant
\underline{n}	[]	Unit vector
P	[Pa]	Pressure
q, \underline{q}	[m/s]	Seepage (free stream) speed, velocity
Q	[m^3/s]	Volume flow
r	[m]	Radial distance, Polar coordinates
Re	[]	Reynolds number
S	[]	Surface
u, \underline{u}	[m/s]	Drift speed, velocity in streamwise direction
U	[m^3]	Volume
v	[m/s]	Speed
V	[m/s]	Average speed
w, \underline{w}	[m/s]	Average pore speed, velocity
\mathcal{W}	[m/s]	Speed of points on S_{fs}
x, y	[m]	Distance, Cartesian coordinates
z	[m]	Linear RUC dimension

Greek Symbols

α	[]	Constant
β	[]	Dimension ratio
Δ	[]	Finite difference operator
ϵ	[]	Porosity, fluid volume/total volume
ε	[<i>m</i>]	Surface roughness
μ	[<i>N · s/m²</i>]	Absolute viscosity
ρ	[<i>kg/m³</i>]	Fluid density
τ	[<i>N/m²</i>]	Local shear stress
ϕ	[<i>rad</i> or °]	Angle, default in radians
χ	[]	Tortuosity
ψ, λ	[...]	Scalar quantities in U_f , units may vary

Miscellaneous

$\langle \rangle$	Phase average operator
$\langle \rangle_f$	Intrinsic phase average operator
$\{ \}$	Deviation operator
∇	Del operator
<u>—</u>	Vector (underlined)
<u><u>—</u></u>	Diadic (double underlined)

Superscripts

$\hat{}$	Flow in streamwise direction
$\tilde{}$	Flow in local channel direction

Subscripts

\parallel	Parallel to streamwise direction
\perp	Perpendicular to streamwise direction
<i>bank</i>	Whole tube bank
<i>avg</i>	Average
<i>f</i>	Fluid, non-stationary matter
<i>ff</i>	Fluid-fluid interface
<i>fs</i>	Fluid-solid interface
<i>m</i>	Relating to tube bank dimension
<i>micro, macro</i>	Microscopic, macroscopic
<i>min, max</i>	Minimum, maximum
<i>o</i>	Solid + fluid matter
<i>p</i>	Pore
<i>s</i>	Solid, stationary matter
<i>SC</i>	Sudden contraction
<i>SE</i>	Sudden expansion
<i>small, large</i>	Small duct, large duct
<i>tube</i>	Tube

Chapter 1

Introduction

A natural starting point for this study is first to define what is meant by a porous medium. Dullien, 1979, gives two criteria of which either one can be used to identify a porous medium. The first is that the material or structure has to contain spaces (voids) which are free of solids. These must be imbedded in the solid or solid matrix. The second criterion is that the solid or solid matrix must be permeable to a fluid(s) in such a way that it must be able to enter at one face and exit at the other.

Flow through porous media was already studied by Henry Darcy in the 1800's (Darcy, 1856). Since that time, numerous modelling studies have been done on porous media with various degrees of empiricisms. During the last two decades a continuum theory for porous media evolved that set the stage for reduction of the empirical basis of porous medium transport equations.

The purpose of this thesis is to describe the application of the continuum flow theory for porous media to selected problem areas in industry. The theory can be applied to both two-dimensional (2D) and three-dimensional (3D) problems, but due to the wide application possibilities, only two-dimensional problems are investigated in this work. The derivation of the continuum flow theory for porous media, to which various people have made valuable contributions over the years, is described in detail by Diedericks, 1999.

In the next part of this chapter, Section 1.1, the history of porous media modelling is briefly

recapped with the emphasis on important historical breakthroughs made during the past two centuries. The last section gives the main characteristics, which can be used to classify a porous medium.

The derivation of the analytical model by Diedericks, 1999, is described in Chapters 2 to 4. The volume averaging method represented in Chapter 2 is based on the concept of Representative Elementary Volumes, better known as REV's. This method for modelling porous media has been used for several years by scientists around the world and provides the basis on which the Navier Stokes transport equation is transformed to be applicable on a macroscopic scale. In Chapter 3, the application of the transport equation to a REV is described, including the concepts of lineality and tortuosity. In the third of the theoretical chapters, Chapter 4, the Representative Unit Cell (RUC) model, based on the REV theory, is described. A RUC model represents the flow characteristics inside a porous medium such that the flow is only along its three Cartesian directions. This provides a method for analyzing the flow characteristics of a porous medium without the use of Computational Fluid Dynamics, better known as CFD, which may be computer intensive due to large matrices that need to be solved.

The first application of the continuum theory for porous media is on cross-flow in tube banks as described in Chapter 5. The results obtained are compared with the experimental results published by e.g. Zukauskas and Ulinskas, 1983. The second application is to a typical stack in timber-drying kilns situated in the southern and eastern parts of South Africa. In this case scale models were built of a timber stack and tested in a wind tunnel. The experimental results generated from the test model, as well as the empirical formula published by Idelchik, 1986, are used for comparison to the theoretical predictions.

1.1 Historical Overview

Darcy's law

An empirical law resembling water flow through a given porous medium was derived by Darcy, 1856, from experimental data. This law states that the flow velocity approaching a

porous medium is proportional to the fluid pressure gradient in the flow direction. Mathematically it can be expressed as:

$$q = -\frac{K}{\mu} \frac{dP}{dx}, \quad (1.1)$$

where q is the superficial speed, K is the Darcy permeability coefficient of the porous medium and μ is the dynamic viscosity of the fluid (Bear, 1972). The pressure loss per unit length is simply written as $\frac{dP}{dx}$ where x is in the streamwise direction. The major shortcoming of this empirical law is that it only applies to creeping flow where mainly viscous effects are responsible for pressure losses. The range of flow velocities where viscous effects are dominant is called the Darcy flow range.

The Forchheimer effect

Reynolds, 1900, formulated that the frictional resistance of the fluid is equal to the sum of two terms. One term is proportional to the fluid speed and the other is proportional to the product of the fluid density and the speed squared. More than 30 years later, Forchheimer, 1937, proposed a deviation, similar to that of Reynolds, 1900, of the Darcy equation to account for the nonlinear behavior evident from experimental results of the intermediate flow range (Bear, 1972). The cause for this nonlinear behavior is today still a debated point with three of them being turbulence, microscopic inertial forces and microscopic drag forces in the interstices of a porous medium as described by Du Plessis and Diedericks, 1999. In mathematical terms, the deviation from the Darcy equation as proposed by Forchheimer, 1937, is

$$-\frac{dP}{dx} = \mathcal{A}q + \mathcal{B}q^n, \quad (1.2)$$

where typically $1.6 < n < 2.0$ in the term, $\mathcal{B}q^n$. The exponential value suggested by Ergun, 1952, is $n = 2$ which is the accepted value used by scientists and engineers when no or inaccurate data is available. Equation 1.2 is not usable without experimental determination of the coefficients \mathcal{A} and \mathcal{B} . These two coefficients were determined empirically in terms of measurable quantities by numerous people. Ergun, 1952, and Bird et al., 1960, give the

most often used results of the coefficients in the equations that follow. The first equation is

$$\mathcal{A} = \frac{150(1 - \epsilon)^2}{\mathcal{D}^2 \epsilon^3} \mu, \quad (1.3)$$

which is generally referred to as the Blake-Kozeny (or Carman-Kozeny) equation with $\mathcal{B} = 0$. The second is,

$$\mathcal{B} = \frac{1.75(1 - \epsilon)}{\mathcal{D} \epsilon^3} \rho, \quad (1.4)$$

better known as the Burke-Plummer equation with $\mathcal{A} = 0$. When Equations 1.3 and 1.4 are substituted into Equation 1.2, the result is

$$-\frac{dP}{dx} = \frac{150(1 - \epsilon)^2}{\mathcal{D}^2 \epsilon^3} \mu q + \frac{1.75(1 - \epsilon)}{\mathcal{D} \epsilon^3} \rho q^2. \quad (1.5)$$

This is known as the Ergun equation (Ergun, 1952) which is commonly used in the chemical engineering industry for design applications when experimental data is not available for a specific porous medium. In the case where reliable data were experimentally obtained, the coefficients of Equation 1.5 can be adjusted as necessary to achieve a good fit with the data.

Recent developments

Considerable work has been done in recent years to improve models for flow through porous media. However, the majority of these are still empirical in nature. Although these models give good results in many applications, it is always better to stay as close to analytical models as possible to have a good understanding of the internal processes involved in the flow. A good example is the RUC model originally developed by Du Plessis and Masliyah, 1988. Two characteristics make this model favourable from a scientific point of view. The first is that both the Navier-Stokes and continuity equations are implemented, although some of the simplifications render the solution to be semi-empirical. The other characteristic is the wide range of applications for which the RUC model is suitable because it is valid for porosities in the range between zero and unity. Examples of these are granular, sponge and fibrous porous media. Some minor improvements have been made to the model, which is published in Du Plessis, 1997. In this thesis, the work focuses on two-dimensional porous media and the RUC model as given by Diedericks, 1999, is used.

1.2 Classification

It is necessary to classify a porous medium according to its physical characteristics as it gives a good indication of the specific model that has to be used for modelling. The interstitial fluid flow is, for example, different between aligned fibrous (2D flow) and granular (3D flow) porous media. The most significant classifications for porous media are briefly described below.

Homogeneous and heterogeneous

According to Bear and Bachmat, 1991, a porous medium of which the physical properties are invariant under translation is classified as *homogeneous*. When at least one of these properties changes with translation, the porous medium is *heterogeneous*. Dullien, 1979, stated that a perfectly homogeneous medium is rarely found and that this criterion can be relaxed, especially when dealing with randomly arranged solids.

Distribution of solid phase

Periodicity in a certain direction regarding the distribution of the solid phase can be either classified as *ordered* (periodic) or *disordered* (random) as described by Quintard and Whitaker, 1994a. The streamwise direction of the solid phase is the most important direction to analyze for periodicity.

Isotropic and anisotropic

An *isotropic* porous medium is defined as one where the physical properties do not vary under rotation. Dullien, 1979, points out that the emphasis here should be on anisotropic characteristics that influence permeability. If this is not the case for all directions of the interstitial flow of the porous medium, it is classified as *anisotropic*.

Structure

The structure of a porous medium does not only depend on the solid material components, but also on the particular manner it is constructed. This is important when analyzing the mechanical properties and flow characteristics. Sand is an example of a *granular* porous medium, but when the granules are *consolidated* the microscopic flow characteristics change and the connectivity, described by Bear and Bachmat, 1991, of the interstices becomes a

major factor in the analysis. *Foam* is sometimes described as a granular porous medium of which the solid and fluid phases are inverted. An artificial sponge is a good example of a foam.

Capillarity

Dullien, 1979, defined a capillary system as one where the solids separating the bulk phases in between have a significant influence in on the physical-chemical state of it due to surface tension. The smaller the distances between the solids in the pores, the greater the capillary effect in the voids. A porous medium where the capillary forces play a significant role is treated differently from one where the voids are large enough that only pressure differences influence the flow.

1.3 Porous Media Modelling Parameters

The choice of parameters chosen to represent the characteristics of a porous medium is crucial to the accuracy of an flow analysis. The basic parameters usually used in modelling include amongst others, length scales, porosity, particle and pore sizes, specific surface areas and tortuosity. Some parameters are interpreted differently among authors, and therefore it is important to follow closely the specific definitions used by each.

Length Scale

Two length scales are always involved when working with porous media. The first is the *macroscopic* length scale, l_{macro} , which is defined as a dimension relating to the physical or arbitrary boundaries, for example, the size of a sponge. The *microscopic* length scale, l_{micro} , on the other hand is the scale relating to the interstices and solid matrix components. It is important to note that the interstitial scale may vary from micrometers as found between sand particles to several meters in large structures, for example, forest tree trunks.

Porosity

Porosity is a parameter extensively used in the analysis of porous media and is the ratio of fluid volume to total (fluid and solid) volume of the medium. The porosity, ϵ , can be

determined experimentally and/or mathematically and is defined as

$$\epsilon \equiv \frac{\text{Fluid volume}}{\text{Total volume}}, \quad (1.6)$$

where $0 \leq \epsilon \leq 1$ and the fluid void volume refer to the connected fluid volume. Pores or parts of pore that do not form part of the macroscopic flow through a porous medium are regarded as part of the solid matrix. The first advantage of the porosity parameter is that it provides a method for classification, e.g. sponges belong to the high porosity group and sand can be anything from medium to very low porosity. Secondly, it gives a good initial indication of the possible flow behavior. A high porosity porous medium usually has a low flow resistance and vice versa.

Note that Equation 1.6 is applied on a macroscopic scale as will be done in Chapter 3. When considering only the porosity of a porous medium, the degree to which the pores are connected with each other to create possible flow paths also need to be taken into account. Dullien, 1979, defined two types of pores that do not contribute to the permeability of the medium. The first are the totally isolated pores. They are easy to ignore as they have no effect on any flowing fluid at all and form part of the solid matrix. The second are so-called dead-end-pores. Experimental determination of porosity, e.g. by immersion of the solid in a liquid, include these dead end pore volumes in the porosity as flow volume. This is not optimal because these pores do not contribute to the macroscopic flow, as the fluid in them is stationary.

Velocity

The definition of a flow velocity in a porous medium is crucial to any analysis attempted. A popular velocity variable is the *superficial* (or *seepage*) velocity, \underline{q} , of which the direction defines the streamwise direction of flow through the medium. The seepage velocity can be visualized as the flow velocity in the absence of the porous medium solid matrix or the velocity at which the fluid approaches the medium. The *interstitial* (or *drift*) velocity, \underline{u} , as defined by Carman, 1937, is the velocity at which the fluid moves from one end of the medium to the other. Both these velocities are strictly in the streamwise direction and

related by the porosity, ϵ , as follows:

$$\underline{q} \equiv \epsilon \underline{u}. \quad (1.7)$$

A third velocity variable that is used in this study is the *average pore velocity*, \underline{w} , described by Carman, 1937, as the actual velocity in the pore channels. If L is defined as the flow path length in the absence of the porous medium and L_e the average effective flow path length inside the porous medium, the following expression is defined:

$$\underline{w} = \underline{u} \frac{L_e}{L}. \quad (1.8)$$

Tortuosity

The ratio $\frac{L_e}{L}$ used above is commonly referred to as the *tortuosity* which is a concept originally used by Carman, 1937. Other definitions for tortuosity also exist, but fall outside the scope of this study.

Pore size

The pore size is a parameter that is difficult to define adequately for a porous medium and is emphasized by Dullien, 1979. A common method is to define a pore size, which is based on the average hydraulic diameter of the microscopic pores through which the flow is moving.

1.4 Two-dimensional Porous Media

For the modelling of flow through porous media with a prismatic layout (two-dimensional flow pattern), several solutions are proposed in the literature. These range from analytical models to totally empirical ones. Examples can be found in Kolodziej, 1986; Sadiq et al, 1995; Du Plessis, 1991; Van der Westhuizen and Du Plessis, 1993; Van der Westhuizen and Du Plessis, 1994; Sangani and Acrivos, 1982; Jackson and James, 1986; Howells, 1998; and Gebart, 1992. However, these solutions are only applicable to the Darcy flow regime where flow velocities are almost non-existent. A theoretical solution that includes both flow

regimes for isotropic porous media is for example the RUC model of Du Plessis and Van der Westhuizen, 1993.

Diedericks, 1999, extended the model of Du Plessis, 1997, which is an updated version of the one by Du Plessis and Van der Westhuizen, 1993, to be applicable to 2D anisotropic porous media. This model of Diedericks, 1999, which is described elsewhere, is used as a basis for this thesis. A very recent publication of Travkin and Catton, 2001, gives a number of solutions for Darcy and Forchheimer flow through different porous media. Although the model is also based on volume averaging theory, the final simplified solutions rely heavily on empirically obtained coefficients. The RUC model on the other hand, tries to eliminate these empiricisms where possible.

Experimental data for flow through two-dimensional porous media is obtained from published data of Zukauskas and Ulinskas, 1983, and experiments conducted during this study.

Chapter 2

Volumetric Averaging with a REV

In this study, a Representative Elementary Volume (REV) is used to model the flow characteristics through a porous medium or homogeneous part thereof. The medium has to consist of a solid matrix with a single fluid inside interconnected voids. By working with averaging operators and Slattery's averaging theorem, two sets of identities are derived which are useful in calculations when the transport equation is applied to the REV. The volumetrically averaged time derivative is also given.

2.1 Representative Elementary Volume

The entity used for averaging is the REV as defined by Bear and Buchlin, 1991, although he was not the first to make use this concept. This macroscopic volume, U_o , is chosen large enough to be statistically representative of the larger medium with respect to both solid, U_s , and fluid, U_f , parts. The general layout of a REV is illustrated in Figure 2.1. The upper volume limit of a REV is the size of the porous medium or homogeneous part thereof, if not entirely homogeneous. This implies that the magnitude of a REV is bounded by the following relation as discussed by Bear and Buchlin, 1991:

$$l_{micro}^3 \ll U_o \ll l_{macro}^3 . \tag{2.1}$$

The variables l_{micro} and l_{macro} are the same as defined in Chapter 1 and illustrated in Figure 2.1.

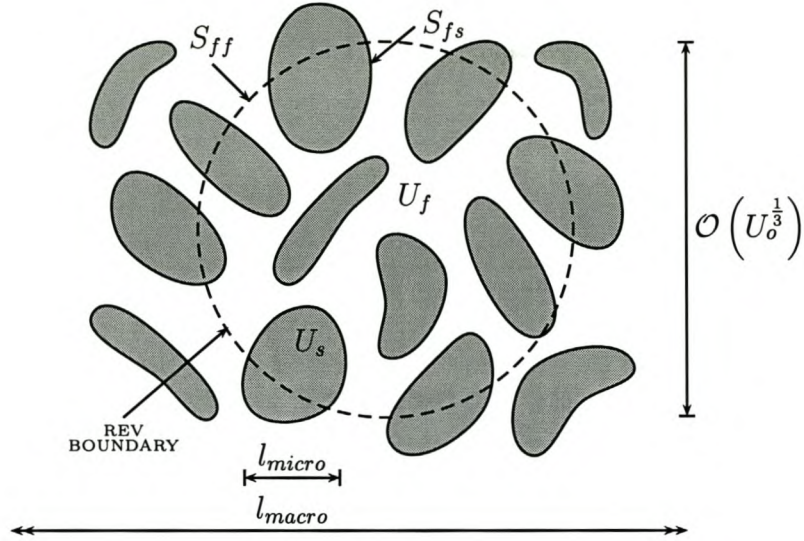


Figure 2.1: Representative Elementary Volume (REV).

Phase average

Two volumetric phase average operators acting on a fluid phase tensor, ψ , defined inside a REV are given in this section. The first is the *intrinsic phase average* operator, $\langle \psi \rangle_f$, defined by

$$\langle \psi \rangle_f \equiv \frac{1}{U_f} \iiint_{U_f} \psi dU \quad (2.2)$$

and the other is the *phase average* operator, $\langle \psi \rangle$, defined as

$$\langle \psi \rangle \equiv \frac{1}{U_o} \iiint_{U_f} \psi dU. \quad (2.3)$$

Using the definition of Equation 1.6, the porosity of a REV is given by

$$\epsilon = \frac{U_f}{U_o}. \quad (2.4)$$

The two phase operators, $\langle \cdot \rangle$ and $\langle \cdot \rangle_f$ can operate on any tensorial quantity ψ . Using the definition of porosity above, it can be deduced that

$$\langle \psi \rangle = \epsilon \langle \psi \rangle_f. \quad (2.5)$$

If $\psi = 1$ it also follows that

$$\langle 1 \rangle_f = 1 \quad \text{and} \quad \langle 1 \rangle = \epsilon. \quad (2.6)$$

Inside a REV at a certain point within U_f , a specific fluid phase property may be different from the phase average for the whole REV. This *deviation*, $\{\psi\}$, is defined as

$$\{\psi\} \equiv \psi - \langle \psi \rangle_f. \quad (2.7)$$

Averaging identities

The averaging operators defined in Equations 2.2 to 2.7 can be used to derive the following identities with α constant and ψ and λ scalar or tensorial fluid quantities:

$$\langle \psi + \lambda \rangle = \langle \psi \rangle + \langle \lambda \rangle \quad (2.8)$$

$$\langle \alpha \psi \rangle = \alpha \langle \psi \rangle \quad (2.9)$$

$$\langle \{\psi\} \rangle = \langle \langle \psi \rangle \rangle = 0 \quad (2.10)$$

$$\{\{\psi\}\} = \{\psi\} \quad (2.11)$$

$$\langle \langle \psi \rangle \rangle = \epsilon \langle \psi \rangle \quad (2.12)$$

$$\langle \{\psi\} \langle \lambda \rangle \rangle = \langle \langle \psi \rangle \{\lambda\} \rangle = 0 \quad (2.13)$$

$$\langle \{\psi\} \{\lambda\} \rangle = \langle \psi \{\lambda\} \rangle = \langle \{\psi\} \lambda \rangle \quad (2.14)$$

$$\langle \psi \lambda \rangle = \langle \psi \rangle \langle \lambda \rangle / \epsilon + \langle \{\psi\} \{\lambda\} \rangle \quad (2.15)$$

$$\{\psi \lambda\} = \{\psi\} \langle \lambda \rangle + \langle \psi \rangle \{\lambda\} + \{\psi\} \{\lambda\} - \langle \{\psi\} \{\lambda\} \rangle. \quad (2.16)$$

2.2 Slattery's Averaging Theorem

Slattery's averaging theorem states the following:

$$\nabla \iiint_{U_f} \psi dU = \iint_{S_{ff}} \underline{n}\psi dS. \quad (2.17)$$

The proof of Slattery's theorem is available in Appendix A. The unit vector, \underline{n} is chosen such that it points outward from the fluid under consideration. This convention is used throughout this thesis. Another theorem that is useful at this stage is the *divergence theorem*. When the latter is applied to a fluid volume, U_f , the result in volume averaged form is:

$$\begin{aligned} \iiint_{U_f} \nabla\psi dU &= \iint_{\partial U_f} \underline{n}\psi dS \\ &= \iint_{S_{fs}} \underline{n}\psi dS + \iint_{S_{ff}} \underline{n}\psi dS. \end{aligned} \quad (2.18)$$

When Equation 2.18 is substituted into the right hand side of Equation 2.17 and dividd with the REV volume U_o , the result is:

$$\frac{1}{U_o} \iiint_{U_f} \nabla\psi dU = \nabla \left(\frac{1}{U_o} \iiint_{U_f} \psi dU \right) + \frac{1}{U_o} \iint_{S_{fs}} \underline{n}\psi dS. \quad (2.19)$$

Equation 2.19 in volume averaged form is

$$\langle \nabla\psi \rangle = \nabla \langle \psi \rangle + \frac{1}{U_o} \iint_{S_{fs}} \underline{n}\psi dS, \quad (2.20)$$

which is known as the spatial averaging theorem. The equations and identities above are also applicable to tensorial quantities such as velocity and are applied as such in the section that follows.

Identities from Slattery's Theorem

Slattery's averaging theorem is frequently applied to volume averaging equations to simplify calculations. The following identities can be derived from the theorem and the averaging

identities in Section 2.1:

$$\langle \nabla \underline{\psi} \rangle = \nabla \langle \underline{\psi} \rangle + \frac{1}{U_o} \iint_{S_{fs}} \underline{n} \underline{\psi} dS \quad (2.21)$$

$$\langle \nabla \cdot \underline{\psi} \rangle = \nabla \cdot \langle \underline{\psi} \rangle + \frac{1}{U_o} \iint_{S_{fs}} \underline{n} \cdot \underline{\psi} dS \quad (2.22)$$

$$\langle \nabla \underline{\psi} \rangle = \epsilon \nabla \langle \underline{\psi} \rangle_f + \frac{1}{U_o} \iint_{S_{fs}} \underline{n} \{ \underline{\psi} \} dS \quad (2.23)$$

$$\langle \nabla \cdot \underline{\psi} \rangle = \epsilon \nabla \cdot \langle \underline{\psi} \rangle_f + \frac{1}{U_o} \iint_{S_{fs}} \underline{n} \cdot \{ \underline{\psi} \} dS \quad (2.24)$$

$$\langle \nabla^2 \underline{\psi} \rangle = \nabla^2 \langle \underline{\psi} \rangle + \frac{1}{U_o} \iint_{S_{fs}} \underline{n} \cdot \nabla \underline{\psi} dS + \frac{1}{U_o} \nabla \cdot \left(\iint_{S_{fs}} \underline{n} \underline{\psi} dS \right) \quad (2.25)$$

$$\nabla \epsilon = -\frac{1}{U_o} \iint_{S_{fs}} \underline{n} dS \quad (2.26)$$

$$\nabla \epsilon = \frac{1}{U_o} \iint_{S_{ff}} \underline{n} dS \quad (2.27)$$

$$\nabla \cdot \langle \{ \underline{\psi} \} \{ \underline{\psi} \} \rangle = \frac{1}{U_o} \iint_{S_{ff}} \{ \underline{\psi} \} \{ \underline{\psi} \} \underline{n} dS \quad (2.28)$$

2.3 Time Derivative

The REV volume, U_o , is considered to be stationary of which the volumes, U_f and U_s , may change shape and magnitude inside its boundaries. The basic time derivative can be written with the Leibniz theorem applied to U_f as follow:

$$\frac{d}{dt} \iiint_{U_f(t)} \psi dU = \iiint_{U_f(t)} \frac{\partial \psi}{\partial t} dU + \iint_{\partial U(t)} \underline{n} \cdot \underline{\mathcal{W}} \psi dS, \quad (2.29)$$

where $\underline{\mathcal{W}}$ is the velocity of points on $\partial U(t)$. The total time derivative can be changed to a partial derivative if U_f is now considered stationary and after rearranging terms it follows that

$$\left\langle \frac{\partial \psi}{\partial t} \right\rangle = \frac{\partial \langle \psi \rangle}{\partial t} - \frac{1}{U_o} \iint_{S_{fs}} \underline{n} \cdot \underline{\mathcal{W}} \psi dS - \frac{1}{U_o} \iint_{S_{ff}} \underline{n} \cdot \underline{\mathcal{W}} \psi dS. \quad (2.30)$$

If the fluid is viscous and a zero slip condition is assumed, the fluid velocity at S_{fs} is the same as the interface itself and therefore $\underline{\mathcal{W}} = \underline{v}$. The interface, S_{ff} , is stationary, which

renders the last term of the equation above to be zero. Equation 2.30 then reduces to:

$$\left\langle \frac{\partial \psi}{\partial t} \right\rangle = \frac{\partial \langle \psi \rangle}{\partial t} - \frac{1}{U_o} \iint_{S_{fs}} \underline{n} \cdot \underline{v} \psi \, dS. \quad (2.31)$$

The time derivative is only given here for completeness. It will be used later at one stage but it is not absolutely necessary, as the final result that is being worked towards is time independent. The identities are used often in the chapter that follows.

Chapter 3

Averaging of Transport Equations

In this chapter the fluid transport equations are applied to the interstitial flow and then averaged to be applicable to a REV. Firstly, the velocity variables necessary to represent the averaged fluid flow for a REV are defined after which the momentum transport and continuity equations are given for the microscopic flow. The averaging theory discussed in Chapter 2 is then applied to these equations which are then suitable for use on a macroscopic scale. The fluid flowing through the porous medium is assumed to be incompressible and Newtonian and this assumption is valid for the remainder of this thesis.

3.1 Volume Averaged Variables

The first variable to be defined in terms of the average over a REV is the seepage velocity as referred to in Chapter 1, namely

$$\underline{q} = \langle \underline{v} \rangle \equiv \frac{1}{U_o} \iiint_{U_f} \underline{v} dU. \quad (3.1)$$

The streamwise unity vector is defined by

$$\hat{n} \equiv \underline{q}/q, \quad (3.2)$$

where the $\hat{\cdot}$ denotes the streamwise direction. The drift velocity is defined similar to \underline{q} as

$$\underline{u} = \langle \underline{v} \rangle_f \equiv \frac{1}{U_f} \iiint_{U_f} \underline{v} dU. \quad (3.3)$$

From Equations 1.6, 3.1 and 3.3 it is clear that

$$\underline{q} = \epsilon \underline{u}, \quad (3.4)$$

which is the same result as given in Chapter 1. The average dynamic fluid pressure for a REV, P_f , in terms of the interstitial fluid pressure, P , is defined as

$$P_f = \langle P \rangle_f \equiv \frac{1}{U_f} \iiint_{U_f} P dU. \quad (3.5)$$

3.2 Conservation of Mass

The microscopic continuity equation can be written as

$$\frac{\partial \rho}{\partial t} + \nabla \cdot (\rho \underline{v}) = 0. \quad (3.6)$$

Since incompressible flow is assumed, the fluid density, ρ , is constant with respect to time and position which renders the first term in Equation 3.6 to be zero. Averaging the remainder of this equation, also utilizing the compressibility assumption above, results in

$$\langle \nabla \cdot \underline{v} \rangle = 0. \quad (3.7)$$

Identity 2.22, together with the no-slip condition at the fluid-solid interface applied to the above equation, yields

$$\nabla \cdot \langle \underline{v} \rangle = 0, \quad (3.8)$$

and applying the definition of Equation 3.1, results in

$$\nabla \cdot \underline{q} = 0. \quad (3.9)$$

3.3 Momentum Transport Equation

The momentum transport equation is used to describe the flow in the interstices of a REV for a given porous medium. In Gibbs notation the momentum equation can be written as

$$\rho \frac{\partial \underline{v}}{\partial t} + \nabla \cdot (\rho \underline{v} \underline{v}) - \rho \underline{g} + \nabla P - \nabla \cdot \underline{\tau} = \underline{0}, \quad (3.10)$$

where \underline{g} is the gravitational force per unit mass. This is a fundamental equation used in the solving of fluid flow problems. The stresses inside the fluid have to be modelled and for a Newtonian fluid

$$\begin{aligned} \underline{\tau} &\propto \nabla \underline{v} \\ &= \mu \left(\nabla \underline{v} + (\nabla \underline{v})^T \right), \end{aligned} \quad (3.11)$$

The second step is possible when $\nabla \underline{v}$ is written as

$$\nabla \underline{v} = \frac{1}{2} \left(\nabla \underline{v} + (\nabla \underline{v})^T \right) + \frac{1}{2} \left(\nabla \underline{v} - (\nabla \underline{v})^T \right), \quad (3.12)$$

where the first term on the right is symmetric and the second term is skew symmetric. It can be proven that the shear tensor, $\underline{\tau}$, has to be symmetric. The skew symmetric term of Equation 3.12 is discarded and replaced with the symmetric part which is the same as the first term. The proportionality constant, μ , also known as the viscosity of the fluid, is always constant for a Newtonian fluid at constant temperature. It is important to note that the fluid density, ρ , is also assumed to be constant, rendering compressibility effects to be

zero. The result of Equation 3.11 applied to the last term of the Navier-Stokes equation, Equation 3.10, yields the following:

$$\begin{aligned}\nabla \cdot \underline{\underline{\tau}} &= \mu (\nabla \underline{\underline{v}} + (\nabla \underline{\underline{v}})^T) \\ &= \nabla \cdot (\mu \nabla \underline{\underline{v}}) + (\nabla \underline{\underline{v}}) \cdot \nabla \mu \\ &= \mu \nabla^2 \underline{\underline{v}}.\end{aligned}\tag{3.13}$$

This leads to a modified momentum equation, better known as the Navier-Stokes equation,

$$\rho \frac{\partial \underline{\underline{v}}}{\partial t} + \nabla \cdot (\rho \underline{\underline{v}} \underline{\underline{v}}) - \rho \underline{\underline{g}} + \nabla P - \mu \nabla^2 \underline{\underline{v}} = \underline{\underline{0}},\tag{3.14}$$

which is valid for incompressible, Newtonian flow. Volume averaging of this equation can be done term for term according to Identity 2.8 as shown in the rest of this section.

Volume averaging of the first term (temporal), using Equation 2.31, results in

$$\left\langle \rho \frac{\partial \underline{\underline{v}}}{\partial t} \right\rangle = \rho \frac{\partial \underline{\underline{q}}}{\partial t},\tag{3.15}$$

where the REV fluid-solid interfaces are stationary and the no-slip condition applies, rendering the boundary velocity to be zero. The convective term (second term in Equation 3.14) is averaged by using Identities 2.15 and 2.22, yielding

$$\begin{aligned}\langle \nabla \cdot (\rho \underline{\underline{v}} \underline{\underline{v}}) \rangle &= \rho \langle \nabla \cdot \underline{\underline{v}} \underline{\underline{v}} \rangle \\ &= \rho \nabla \cdot (\underline{\underline{q}} \underline{\underline{q}} / \epsilon) + \rho \nabla \cdot \langle \{ \underline{\underline{v}} \} \{ \underline{\underline{v}} \} \rangle.\end{aligned}\tag{3.16}$$

The gravitational term, $\rho \underline{\underline{g}}$, is simply averaged with Equation 2.3 and Identity 2.9 as follows:

$$\begin{aligned}\langle \rho \underline{\underline{g}} \rangle &= \rho \langle \underline{\underline{g}} \rangle \\ &= \epsilon \rho \underline{\underline{g}}.\end{aligned}\tag{3.17}$$

The pressure term, ∇P , in the averaged form with Identity 2.23 applied, reduces to

$$\langle \nabla P \rangle = \epsilon \nabla P_f + \frac{1}{U_o} \iint_{S_{fs}} \underline{n} \{P\} dS, \quad (3.18)$$

where $P_f = \langle P \rangle_f$. With the help of Identity 2.25 the last term of Equation 3.14 is averaged as follows:

$$\begin{aligned} \langle \mu \nabla^2 \underline{v} \rangle &= \mu \nabla^2 \langle \underline{v} \rangle + \frac{1}{U_o} \iint_{S_{fs}} \underline{n} \cdot \nabla \underline{v} dS + \frac{1}{U_o} \nabla \cdot \left(\iint_{S_{fs}} \underline{n} \underline{v} dS \right) \\ &= \mu \nabla^2 \underline{q} + \frac{1}{U_o} \iint_{S_{fs}} \underline{n} \cdot \nabla \underline{v} dS. \end{aligned} \quad (3.19)$$

The integral terms in Equations 3.18 and 3.19 cannot be solved in terms of macroscopic parameters and therefore the RUC model as done Chapter 4 is used which result in the closure of the Navier-Stokes equation.

If Equations 3.15 to 3.19 are combined into Equation 3.14, the result is

$$\begin{aligned} \rho \frac{\partial \underline{q}}{\partial t} + \rho \nabla \cdot (\underline{q} \underline{q} / \epsilon) + \rho \nabla \cdot \langle \{ \underline{v} \} \{ \underline{v} \} \rangle + \epsilon \nabla P_f - \epsilon \rho \underline{g} - \mu \nabla^2 \underline{q} \\ + \frac{1}{U_o} \iint_{S_{fs}} (\underline{n} \{P\} - \mu \underline{n} \cdot \nabla \underline{v}) dS = \underline{0}. \end{aligned} \quad (3.20)$$

The averaged and time independent form of the momentum equation, where \underline{q} assumed to be constant with respect to time and space, Equation 3.20 can be written as

$$-\epsilon \nabla P_f = \rho \nabla \cdot \langle \{ \underline{v} \} \{ \underline{v} \} \rangle + \frac{1}{U_o} \iint_{S_{fs}} (\underline{n} \{P\} - \mu \underline{n} \cdot \nabla \underline{v}) dS. \quad (3.21)$$

Here the gravitation term is included in the pressure term as a pressure head.

Equation 3.21 is the final result obtained by applying the volume averaging theory to the general Navier-Stokes equation as given in Equation 3.14 for steady incompressible Newtonian flow. Equations 3.20 and 3.21 are valid for any degree of anisotropy. In this thesis, closure of the time independent case is done by modelling with representative unit cells (RUC's) in Chapter 4.

3.4 Interstitial Streamwise Transport

The interstitial velocity field of a REV with no dead ends is shown in Figure 3.1. As previously defined, \underline{q} is the fluid velocity in the streamwise direction with \hat{n} defined as the constant unit vector in the same direction and \tilde{n} the unit vector tangent to streamline directions within U_f . The unit vector \underline{n} is normal to S_{fs} and S_{ff} as shown in Figure 3.1, always pointing outward from U_f by convention. The *effective interstitial velocity*, \tilde{w} , which has a constant magnitude within the REV, is defined such that

$$\begin{aligned} \tilde{w} \hat{n} \cdot \iiint_{U_f} \tilde{n} dU &\equiv \iiint_{U_f} \underline{v} dU \\ &= U_f \langle \underline{v} \rangle_f. \end{aligned} \quad (3.22)$$

It is important to realize that \tilde{w} is only an estimate value calculated from the \underline{v} field and cannot be measured directly as is the case with \underline{q} .

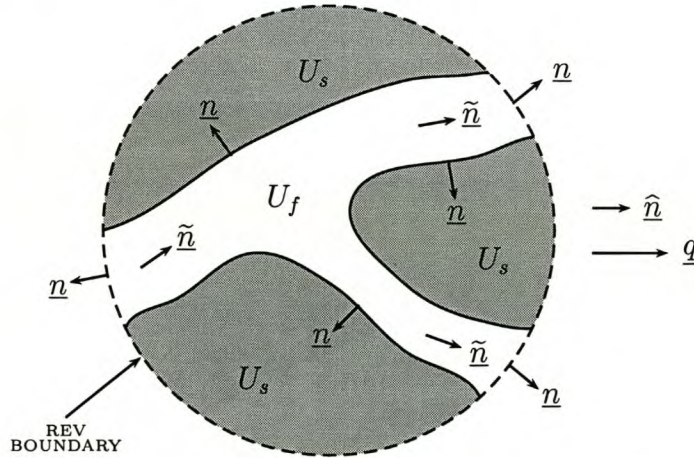


Figure 3.1: Representative Elementary Volume (REV).

If the *effective streamwise volume* is defined as

$$U_{||} = \iiint_{U_f} \tilde{n} \cdot \hat{n} dU, \quad (3.23)$$

then equation 3.22 can be transformed as follows

$$\hat{w} \equiv \tilde{w}\hat{n} = \frac{1}{U_{\parallel}} \iiint_{U_f} \underline{v} dU = \frac{U_f}{U_{\parallel}} \langle \underline{v} \rangle_f = \frac{U_f}{U_{\parallel}} \underline{u}, \quad (3.24)$$

where \hat{w} is the *streamwise average pore speed*.

3.5 Lineality and Tortuosity

The symmetrical form of $\hat{n}\hat{n}$ enables the dot product to be used commutatively as

$$\hat{n}\hat{n} \cdot \tilde{n} = \tilde{n} \cdot \hat{n}\hat{n}. \quad (3.25)$$

This makes it possible to write Equation 3.22 as

$$\langle \underline{v} \rangle_f = \hat{w} \cdot \frac{1}{U_f} \iiint_{U_f} \tilde{n}\hat{n} dU. \quad (3.26)$$

The *geometric lineality diadic* can now be defined as

$$\underline{\underline{\mathcal{L}}} \equiv \frac{1}{U_f} \iiint_{U_f} \tilde{n}\hat{n} dU. \quad (3.27)$$

Equation 3.26 expressed in terms of the superficial velocity and geometric lineality is

$$\underline{q} = \langle \underline{v} \rangle = \epsilon \hat{w} \cdot \underline{\underline{\mathcal{L}}}. \quad (3.28)$$

With \underline{q} and \hat{w} both streamwise vectors. Equation 3.28 can be expressed as

$$\underline{q} = \underline{q} \cdot \hat{n} = \epsilon \hat{w}\hat{n} \cdot \underline{\underline{\mathcal{L}}} \cdot \hat{n} = \epsilon \hat{w}\mathcal{L}, \quad (3.29)$$

where \mathcal{L} is defined as the (*streamwise*) *lineality*. It is now convenient to write the lineality in terms of the following variables obtained from Equations 3.24 to 3.29 yielding

$$\mathcal{L} = \frac{u}{\hat{w}} = \frac{q}{\epsilon\hat{w}} = \frac{U_{\parallel}}{U_f}. \quad (3.30)$$

The *tortuosity tensor*, $\underline{\underline{\chi}}$, in terms of the geometric lineality is defined as

$$\underline{\underline{\chi}} \cdot \underline{\underline{\mathcal{L}}} \equiv \underline{\underline{1}}. \quad (3.31)$$

Taking the dot product of 3.28 and $\underline{\underline{\chi}}$, produces the following result:

$$\underline{q} \cdot \underline{\underline{\chi}} = \epsilon\hat{w}. \quad (3.32)$$

As done in the case of lineality in Equation 3.29, it can be deduced that the tortuosity scalar, χ , in terms of convenient scalars is

$$\chi = \frac{\epsilon\hat{w}}{q} = \frac{U_f}{U_{\parallel}}. \quad (3.33)$$

Chapter 4

Closure Modelling With a RUC

The concept of the Representative Unit Cell or RUC, as originally developed by Du Plessis and Masliyah, 1988, for foam was extended in the work of Diedericks, 1999, to apply to anisotropic media. In this chapter the work of Diedericks, 1999, is recapped with the emphasis on two-dimensional anisotropic porous media. The flow is restricted to two of the principal Cartesian axes of the RUC. The first step is to define the RUC, after which the specific parameters are applied to the averaged transport equation described in Chapter 3. The result is a RUC based flow equation for 2D anisotropic porous media with the isotropic model as a special case of the anisotropic one.

4.1 A RUC for Anisotropic Fibres

The main advantage of a RUC is that both geometric and flow characteristics are modelled to fit along the three main Cartesian directions which significantly simplifies the flow problem to be solved. In the two-dimensional case two totally different flow situations are possible, one being along the prismatic structure and the other perpendicular to it. These two cases should be solved differently but only the latter case, shown in Figure 4.1, is analyzed in this chapter as it is applicable to the investigations of Chapters 5 and 6.

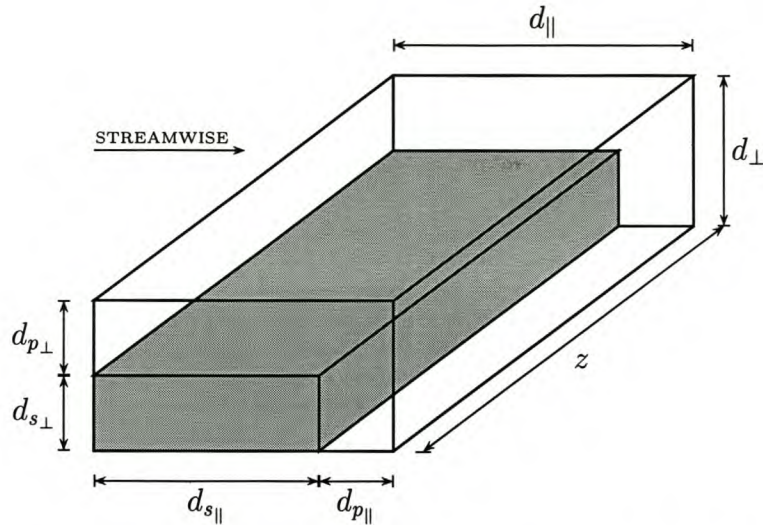


Figure 4.1: RUC for a two-dimensional anisotropic fibre bed.

The properties of a RUC with respect to the original REV of the porous medium are summarized by Diedericks, 1999, of which the first is that the porosities are to be exactly the same. If this is not the case, the volumes through which fluid can pass through cannot be the same and would therefore create significant inaccuracies in the RUC model. Secondly, the solids and voids in the RUC are to be arranged in a rectangular fashion such that they basically represent the original porous matrix properties. The principal Cartesian directions of a RUC are chosen such that they coincide with the rectangular solid geometry. Inside and on the borders of a RUC the fluid-solid surfaces should be configured in pair-wise sets of parallel surfaces. Diedericks, 1999, allow for some lateral displacement of these surfaces. This rectangular fashion of the solids in the model ensures that the flow is only along the principal directions of the RUC. It has to be emphasized that the RUC is not necessarily a building block of the porous medium solid matrix, but it resembles the flow characteristics including interconnectedness. Further simplicity is obtained when the RUC is constructed such that the streamwise direction is parallel to one of the principal axes of the RUC. Diedericks, 1999, points out that in some anisotropic applications, the direction of discharge may not be in the same direction as the applied pressure gradient. Under these circumstances it would then be appropriate to align the geometry of the RUC with that of the solid matrix only and not the streamwise direction.

To ensure that the porous medium is two-dimensional, it is necessary that $z \gg d_{\parallel}$ and $z \gg d_{\perp}$ where d_{\parallel} , d_{\perp} and z are the side lengths of the RUC as in Figure 4.1. The dimensions of the RUC solid are $d_{s_{\parallel}} \times d_{s_{\perp}} \times z$. Channel widths, $d_{p_{\parallel}}$ and $d_{p_{\perp}}$, are respectively in the x_{\perp} and x_{\parallel} directions along which the flow is guided by the neighboring solids. The volumetric characteristics as defined in Chapter 2 are as follows for the 2D anisotropic RUC:

$$U_o = d_{\parallel}d_{\perp}z \quad , \quad U_f = \epsilon d_{\parallel}d_{\perp}z \quad , \quad U_s = (1 - \epsilon)d_{\parallel}d_{\perp}z \quad (4.1)$$

and

$$\epsilon = 1 - \frac{d_{s_{\parallel}}d_{s_{\perp}}}{d_{\parallel}d_{\perp}}. \quad (4.2)$$

The effective streamwise flow area, which is perpendicular to the streamwise direction, is defined as

$$A_{\perp} \equiv d_{p_{\perp}}z. \quad (4.3)$$

Similarly, the effective flow area in the transverse channel is

$$A_{\parallel} \equiv d_{p_{\parallel}}z. \quad (4.4)$$

The average channel speeds in the RUC parallel and transverse to the streamwise direction are

$$v_{\parallel avg} = V_{\parallel} = \hat{w} \quad \text{and} \quad v_{\perp avg} = V_{\perp} = \beta \hat{w} \quad (4.5)$$

respectively, with the channel anisotropic factor, β , defined as

$$\beta \equiv \frac{d_{p_{\perp}}}{d_{p_{\parallel}}} = \frac{A_{\perp}}{A_{\parallel}} = \frac{V_{\perp}}{V_{\parallel}}. \quad (4.6)$$

The value of β is such that volume flow in both the streamwise and transverse channels are equal. Equation 4.6 only applies to 2D prismatic RUC's and therefore does not necessarily hold for porous media without a prismatic structure. The tortuosity in terms of the RUC dimensions is

$$\chi = \frac{d_{\parallel}d_{\perp} - d_{s\parallel}d_{s\perp}}{d_{\parallel}d_{p\perp}}, \quad (4.7)$$

by using Equation 3.33.

4.2 Closure

The unsolved integral term of the volume averaged time-independent Navier-Stokes equation, Equation 3.21, will now be solved using the anisotropic RUC (Figure 4.1) for the Darcy and Forchheimer flow regimes.

In the Darcy flow regime, the frictional forces on the fluid-solid interfaces are the primary cause for pressure losses through the porous medium. Typical streamlines are shown in Figure 4.2. It is assumed that as $Re \Rightarrow 0$, the first term on the right hand side of Equation 3.21 becomes insignificant which leaves us with only one integral to solve. An assumption is made by replacing the $\underline{n}\{P\}$ term inside the integral with the shear stresses encountered by the fluid in the transverse channel, because the pressure loss in the transverse channel is equal to the wall shear stresses on the sides of the channel. Note that the wall shear stresses in the transverse channel include both S_{\perp} surfaces as shown in Figure 4.2 and it is assumed that ∇P_f is in the streamwise direction. The result is that the pressure loss in the transverse channel is added to that of the streamwise channel. This changes Equation 3.21 to

$$\epsilon \nabla P_f = \frac{\mu}{U_o} \hat{\underline{n}} \iint_{S_{\parallel}} \underline{n} \cdot \nabla v_{\parallel} dS + \frac{\mu}{U_o} \hat{\underline{n}} \iint_{S_{\perp}} \underline{n} \cdot \nabla v_{\perp} dS. \quad (4.8)$$

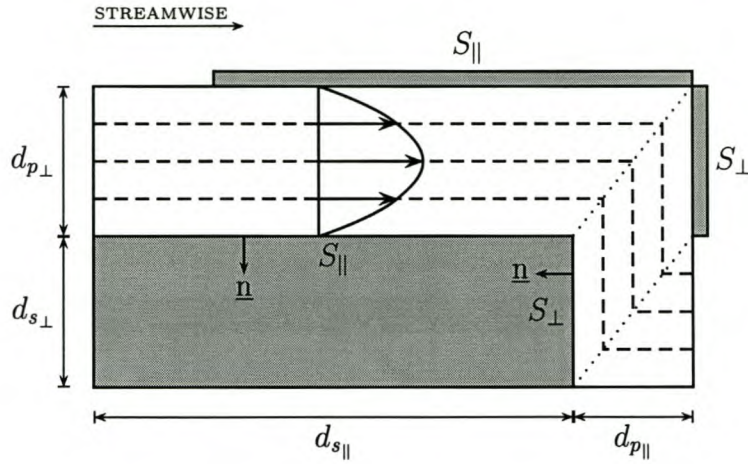


Figure 4.2: Streamlines in a two-dimensional anisotropic RUC for the Darcy flow range.

If the flow in the channels is assumed to be fully developed laminar viscous flow as shown in Figure 4.2, the frictional forces would be constant over both S_{\parallel} and S_{\perp} surfaces although not necessarily equal. This enables the two surface integrals of Equation 4.8 to be written in terms of the variables in Figure 4.2 and the specific channel velocities as follows:

$$\epsilon \nabla P_f = -\frac{2\mu d_{s\parallel} z}{U_o} \left(\frac{\partial v_{\parallel}}{\partial y} \right)_{S_{\parallel}} \hat{n} - \frac{2\mu d_{s\perp} z}{U_o} \left(\frac{\partial v_{\perp}}{\partial x} \right)_{S_{\perp}} \hat{n}. \quad (4.9)$$

It is now assumed that the all flow in the channels can be modelled with fully developed laminar Newtonian flow between infinitely large parallel plates, better known as plane Poiseuille flow. This model is described in Appendix B. When the plane Poiseuille flow results, Equation B.4, is applied to Equation 4.9, the result is

$$\epsilon \nabla P_f = -\frac{12\mu z \hat{w}}{U_o} \left(\frac{d_{s\parallel}}{d_{p\perp}} + \beta \frac{d_{s\perp}}{d_{p\parallel}} \right) \hat{n}, \quad (4.10)$$

where the average velocities were replaced using Equation 4.5. The next step is to obtain the pressure gradient in terms of the seepage speed and this is done using the tortuosity constant of Equation 3.33, yielding

$$\epsilon \nabla P_f = -\frac{12\mu z \chi q}{\epsilon U_o} \left(\frac{d_{s\parallel}}{d_{p\perp}} + \beta \frac{d_{s\perp}}{d_{p\parallel}} \right) \hat{n}. \quad (4.11)$$

This is the final result for the Darcy flow regime using the RUC model.

To calculate the flow for the Forchheimer region, three assumptions are used. First, the drag of the solid part inside the RUC now plays a dominating role, rendering the shear stresses to be insignificant. Another assumption is that a recirculation zone is created downstream of the solid material by the inertial effect, which is illustrated in Figure 4.3. Subscripts (*a*), (*b*) and (*c*) denote the upstream surface, downstream surface and streamline inflection point respectively. The third assumption is that the opposing pressure forces on the streamwise surfaces of the solid cancel out due to symmetric flow around the solid.

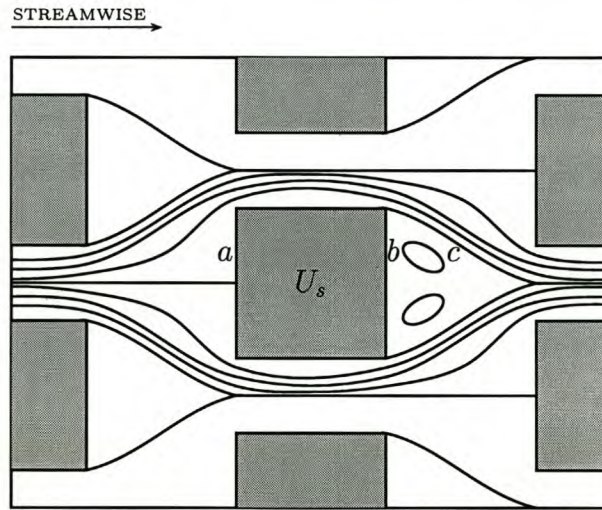


Figure 4.3: *Interstitial laminar flow with recirculation for a two-dimensional RUC (not an exact solution).*

Equation 3.21 is also the departure point for flow in the Forchheimer region. As done by Diedericks, 1999, the first term on the right of Equation 3.21 can be written as

$$\rho \nabla \cdot \langle \{\underline{v}\} \{\underline{v}\} \rangle = \frac{\rho}{U_o} \iint_{S_{ff}} \{\underline{v}\} \{\underline{v}\} \underline{n} dS, \quad (4.12)$$

by using Identity 2.28 obtained from Slattery's averaging theorem. It can be reasoned that the fluid flow exiting one RUC is exactly the same as that entering the next one, and this consequently also applies to the velocity deviations. This implies that the surface integral in Equation 4.12 is zero.

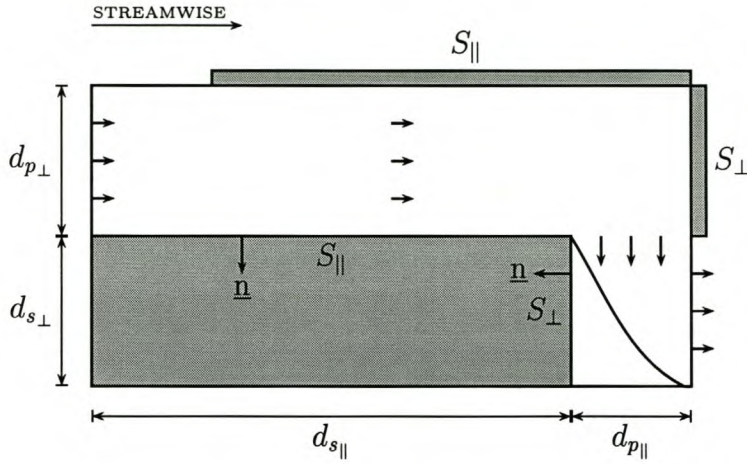


Figure 4.4: Two-dimensional anisotropic RUC for the Forchheimer flow range.

The remaining term to be solved in Equation 3.21 is

$$\epsilon \nabla P_f = -\frac{1}{U_o} \iint_{S_{fs}} \underline{n} \{P\} dS. \quad (4.13)$$

Diedericks, 1999, discusses three possible solutions for this equation. The first solution is obtained by initially writing Equation 4.13 as

$$\begin{aligned} \epsilon \nabla P_f &= -\frac{1}{U_o} \left[\iint_{S_{\perp}(a)} \hat{n} P dS - \iint_{S_{\perp}(a)} \hat{n} \langle P \rangle_f dS + \iint_{S_{\perp}(b)} \hat{n} P dS - \iint_{S_{\perp}(b)} \hat{n} \langle P \rangle_f dS \right] \\ &= -\frac{1}{U_o} \left[\iint_{d_{s_{\perp}(a)}} \hat{n} P dS - \langle P \rangle_f d_{s_{\perp}(a)} + \iint_{S_{\perp}(b)} \hat{n} P dS + \langle P \rangle_f d_{s_{\perp}(b)} \right] \\ &= -\frac{1}{U_o} \left[\iint_{S_{\perp}(a)} \hat{n} P dS + \iint_{S_{\perp}(b)} \hat{n} P dS \right], \end{aligned} \quad (4.14)$$

where subscripts (a) and (b) denote the respective positions shown in Figure 4.3. The $\langle P \rangle_f$ terms cancel out because $d_{s_{\perp}(a)} = d_{s_{\perp}(b)}$. If Bernoulli's equation is applied along the dividing streamline between the stagnation point at (a) and the streamline inflection point at (c) in Figure 4.3, the result is

$$P_{(a)} = \frac{1}{2} \rho v_{(c)}^2 + P_{(c)}, \quad (4.15)$$

where the flow is assumed to be steady state and inviscid with gravitational effects already cancelled out with the corresponding pressures induced. The pressure at the inflection point, (c), is used because it is where the pressure gradient perpendicular to the streamline between the recirculation zone and the flow on the other side is zero. If the pressure at surface (a) in Figure 4.3 is assumed to be uniform on the surface, the two integrals of Equation 4.14 can be solved and then

$$\epsilon \nabla P_f = -\frac{z}{U_o} \left(P_{(a)} d_{s_{\perp}(a)} \hat{n} - P_{(c)} d_{s_{\perp}(b)} \hat{n} \right). \quad (4.16)$$

Substituting Equation 4.15 in Equation 4.16 yields

$$\begin{aligned} \epsilon \nabla P_f &= -\frac{z}{U_o} P_{(a)} d_{s_{\perp}(a)} \hat{n} - \frac{z}{U_o} \left(\frac{1}{2} \rho v_{(c)}^2 - P_{(a)} \right) d_{s_{\perp}(b)} \hat{n} \\ &= -\frac{z}{2U_o} \rho v_{(c)}^2 d_{s_{\perp}} \hat{n}. \end{aligned} \quad (4.17)$$

There are three models as a result of how $v_{(c)}$ is interpreted and all three are given below. These receive attention again when they are compared with experimental data. The speed, $v_{(c)}$, at the inflection point is approximated by Diedericks, 1999, to be equal to the transverse speed, V_{\perp} , and implies that

$$v_{(c)} \approx V_{\perp} = \beta \hat{w}. \quad (4.18)$$

This approximation leads to a solution of the original Equation 3.21 in terms of the physical dimensions of the RUC shown in Figure 4.4, as follows:

$$\epsilon \nabla P_f = -\frac{\rho \beta^2 d_{s_{\perp}} z \hat{w}^2}{2U_o} \hat{n}. \quad (4.19)$$

Using the tortuosity from Equation 3.33 the first result is:

$$\epsilon \nabla P_f = -\frac{\rho \chi^2 \beta^2 d_{s_{\perp}} z q^2}{2\epsilon^2 U_o} \hat{n}. \quad (4.20)$$

The second solution is obtained when the recirculation and momentum loss is viewed as a pressure drag acting across the solid of each RUC. For a single object in a uniform flow field, the pressure drag is always a function of the free stream speed. Analogous to this, the ‘free stream’ speed flowing around a solid of a RUC can be approximated with V_{\parallel} ($V_{\parallel} = \hat{w}$), which is an obvious value to use. The pressure loss using this model is represented by

$$\begin{aligned}\epsilon \nabla P_f &= -\frac{1}{2U_o} \rho C_D \hat{w}^2 d_{s\perp} z \hat{n} \\ &= -\frac{\rho \chi^2 C_D d_{s\perp} z q^2}{2\epsilon^2 U_o} \hat{n},\end{aligned}\tag{4.21}$$

where C_D is the drag coefficient of the solid in the RUC or that of the original body shape encountered in the porous medium. It can be reasoned that the approximation of the free stream speed is closer to V_{\perp} ($V_{\perp} = \beta \hat{w}$) and consequently the third solution is:

$$\epsilon \nabla P_f = -\frac{\rho \chi^2 \beta^2 C_D d_{s\perp} z q^2}{2\epsilon^2 U_o} \hat{n}.\tag{4.22}$$

The value to be used for C_D can be obtained from flow data around a single object from various sources, of which White, 1994, is a good example. The specific shape used to determine C_D can either be that of the RUC solid or the actual shape of a single 2D fibre or column of the porous medium. The shape could for instance be spherical or cubic in the case of sand particles, although spherical is preferred as it more closely resembles the original structure.

4.3 Asymptote Matching

Asymptote matching of expressions valid for two opposing ranges as described by Churchill and Usagi, 1972, is a procedure used to produce a combined result which is valid for both. This is applied to the results for the Darcy and Forchheimer flow ranges obtained in this chapter. The applicable format in this case is

$$f(q) = \left((\mathcal{A}q)^s + (\mathcal{B}q^2)^s \right)^{\frac{1}{s}},\tag{4.23}$$

where \mathcal{A} , \mathcal{B} and s are constants. The latter of these constants is called the shifting parameter, which is dependent on the specific process (Van der Westhuizen and Du Plessis, 1994). The appropriate value for s is $s = 1$, as it gives acceptable results when compared with experimental data. Equations 4.11, 4.20, 4.21 and 4.22 combined with 4.23 result in the following:

$$\epsilon \nabla P_f = -\frac{12\mu\chi zq}{\epsilon U_o} \left(\frac{d_{s\parallel}}{d_{p\perp}} + \beta \frac{d_{s\perp}}{d_{p\parallel}} \right) \hat{n} - \frac{\rho\chi^2\beta^2 d_{s\perp} zq^2}{2\epsilon^2 U_o} \hat{n} \quad (4.24)$$

$$\epsilon \nabla P_f = -\frac{12\mu\chi zq}{\epsilon U_o} \left(\frac{d_{s\parallel}}{d_{p\perp}} + \beta \frac{d_{s\perp}}{d_{p\parallel}} \right) \hat{n} - \frac{\rho\chi^2 C_D d_{s\perp} zq^2}{2\epsilon^2 U_o} \hat{n} \quad (4.25)$$

$$\epsilon \nabla P_f = -\frac{12\mu\chi zq}{\epsilon U_o} \left(\frac{d_{s\parallel}}{d_{p\perp}} + \beta \frac{d_{s\perp}}{d_{p\parallel}} \right) \hat{n} - \frac{\rho\chi^2\beta^2 C_D d_{s\perp} zq^2}{2\epsilon^2 U_o} \hat{n}. \quad (4.26)$$

4.4 Friction Factor and Reynolds Number

When theoretical solutions and experimental data are evaluated, it is always convenient to do it with dimensionless parameters. When the pressure loss or resistance across a medium needs to be related with the flow rate, one of two routes is usually taken to determine a meaningful friction factor.

The first option is to use the definition by Shah and London, 1979, where the friction factor is defined as the ratio of the wall shear stress to the flow kinetic energy per unit volume. This factor is called the Fanning friction factor for fully developed flow in a duct and is given by Shah and London, 1979, as:

$$\begin{aligned} f &= -\frac{dP}{dx} \frac{2r_h}{g\rho V^2} \\ &= -\frac{dP}{dx} \frac{d_h}{2g\rho q_{avg}^2}. \end{aligned} \quad (4.27)$$

where V is the free stream speed and r_h and d_h is the hydraulic radius and hydraulic diameter respectively. A variation of this, the Darcy friction factor, is defined as

$$f_D = -\frac{dP}{dx} \frac{2d_h}{g\rho q_{avg}^2}, \quad (4.28)$$

with the only difference the characteristic dimensions r_h and d_h . Either of the above friction factor definitions can be applied to porous media because they only differ by a constant factor of 4 and the important thing is that the reader should which one is used. Instead of referring to a characteristic dimension of the cross-sectional flow area, a dimension of the solid matrix is used. The void size is then considered to be a function of porosity as it is more likely to be varied than the granular or fibre size of the solid matrix. Practical examples would be the variable fibre density in air filters that can all be evaluated against the same characteristic fibre thickness or different tube configurations in heat exchangers. The critical factors that influence flow resistance in a porous medium are the fluid and solid areas perpendicular to the streamwise direction. Consequently, the appropriate RUC dimension D is to be used as frictional characteristic dimension for cylindrical prismatic porous media in cross flow (e.g. see Figures 5.1 and 5.2). A modified Fanning friction factor for 2D porous media, as given by Dullien, 1979, is

$$f = -\frac{dP}{dx} \frac{D}{2g\rho q^2}. \quad (4.29)$$

The second option for a friction factor is one that originates from the Darcy law, Equation 1.1. If a frictional coefficient for porous media is defined as $F = \epsilon/K$, the Darcy law can be changed to

$$F = -\frac{\epsilon}{\mu q} \frac{dP}{dx}, \quad (4.30)$$

as done for example by Du Plessis, 1997. The units of F is $[m^{-2}]$ and to obtain a dimensionless form, Equation 4.30 can be multiplied by the square of a characteristic solid matrix or RUC dimension. For cylinders in tube banks the characteristic reference dimension, D , is used and where the solids are not circular, the RUC dimension, $d_{s\perp}$, is used, respectively yielding

$$FD^2 = -\frac{\epsilon D^2}{\mu q} \frac{dP}{dx}$$

and

$$F d_{s\perp}^2 = -\frac{\epsilon d_{s\perp}^2}{\mu q} \frac{dP}{dx}. \quad (4.31)$$

In this thesis the friction factor for porous media, F , as in Equation 4.30 is used. Consequently when Equation 4.31 is applied to Equations 4.24 to 4.26 they become

$$F d_{s\perp}^2 = \frac{12\chi z d_{s\perp}^2}{\epsilon U_o} \left(\frac{d_{s\parallel}}{d_{p\perp}} + \beta \frac{d_{s\perp}}{d_{p\parallel}} \right) + \frac{\chi^2 \beta^2 z d_{s\perp}^2 Re_{qd_{s\perp}}}{2\epsilon^2 U_o} \quad (4.32)$$

$$F d_{s\perp}^2 = \frac{12\chi z d_{s\perp}^2}{\epsilon U_o} \left(\frac{d_{s\parallel}}{d_{p\perp}} + \beta \frac{d_{s\perp}}{d_{p\parallel}} \right) + \frac{\chi^2 C_D z d_{s\perp}^2 Re_{qd_{s\perp}}}{2\epsilon^2 U_o} \quad (4.33)$$

$$F d_{s\perp}^2 = \frac{12\chi z d_{s\perp}^2}{\epsilon U_o} \left(\frac{d_{s\parallel}}{d_{p\perp}} + \beta \frac{d_{s\perp}}{d_{p\parallel}} \right) + \frac{\chi^2 \beta^2 C_D z d_{s\perp}^2 Re_{qd_{s\perp}}}{2\epsilon^2 U_o}. \quad (4.34)$$

When necessary, the characteristic dimension can be changed to another by simply changing the $d_{s\perp}^2$ factors in all instances in the set of equations above.

The most popular dimensionless form to express the flow rate of viscous fluids is the Reynolds number defined for a 2D RUC as:

$$Re_{qd_{s\perp}} = \frac{\rho q d_{s\perp}}{\mu}. \quad (4.35)$$

To avoid confusion, the two subscripts which are inserted after the Re symbol, denoting the specific input values for speed and linear characteristic dimension used to calculate the value of the Reynolds number. The comparison of results between Equations 4.32, 4.33 and 4.34, is done in Chapter 6.

Chapter 5

Cross-flow in Tube Banks

An analysis of cross-flow in tube banks (or arrays) as done by Zukauskas and Ulinskas, 1983, incorporates various experiments undertaken to give engineers some empirical mathematical tools to aid in the design of, for example, heat exchangers. Various differences in designs are covered for by Zukauskas and Ulinskas, 1983, including square, staggered and inclined arrays. The goal of this chapter is to compare the empirical results of Zukauskas and Ulinskas, 1983, with the current theory as derived in Chapter 4. From these comparative results, it is clear that it is not necessary to use fully empirical models, but to do calculations from first principles with as few assumptions as possible.

In the first part of this chapter the work of Zukauskas and Ulinskas, 1983, is recapped and presented in such a manner as to comply with the notation used in previous chapters. The results of Zukauskas and Ulinskas, 1983, are based on experimental results of cross-flow through arrays of cylinders to which the authors fitted a variety of curves. Section 5.3 deals with the application of the RUC model to both staggered and square cylinder arrays. These results are compared with those of Zukauskas and Ulinskas, 1983, in Section 5.4.

The RUC theory derived in Chapter 4 is applied to two of the infinite number of possible tube configurations. These are geometrically specified staggered and square arrays where the flow is perpendicular to the tubes in a specific direction. When only a few tube rows are present, microscopic effects become significant in the macroscopic analysis and correction

factors are given by Zukauskas and Ulinskas, 1983, to adjust calculated values. The RUC theory as derived in Chapter 4 makes no provision for this and therefore only banks with a sufficient number of rows are considered where entrance and wall effects are negligible in the macroscopic environment. From the data of Zukauskas and Ulinskas, 1983, it is evident that with a tube array of more than 7×7 rows for staggered and 30×30 rows for square banks, the total error is less than 10% compared to the case with an infinite number of tubes. This is valid for the range $10 \leq Re_{V_{max}D} \leq 10^6$. The variable V_{max} is defined in Equations 5.2 and 5.3 and D in Figures 5.1 and 5.2.

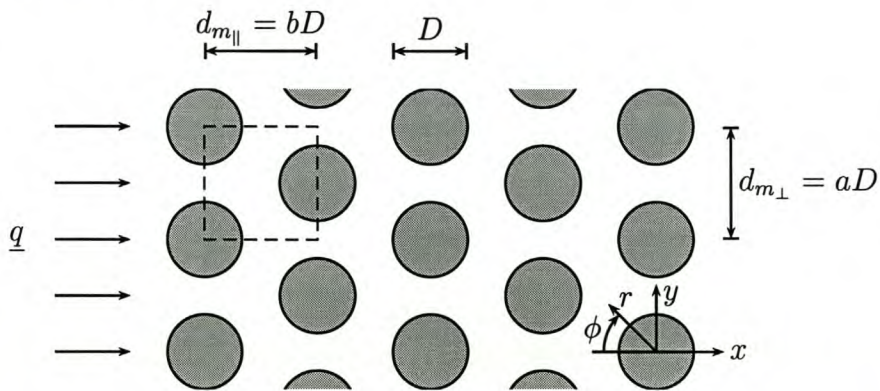


Figure 5.1: Illustration of a staggered array with the area inside the dashed line, showing the size of the smallest periodic volume.

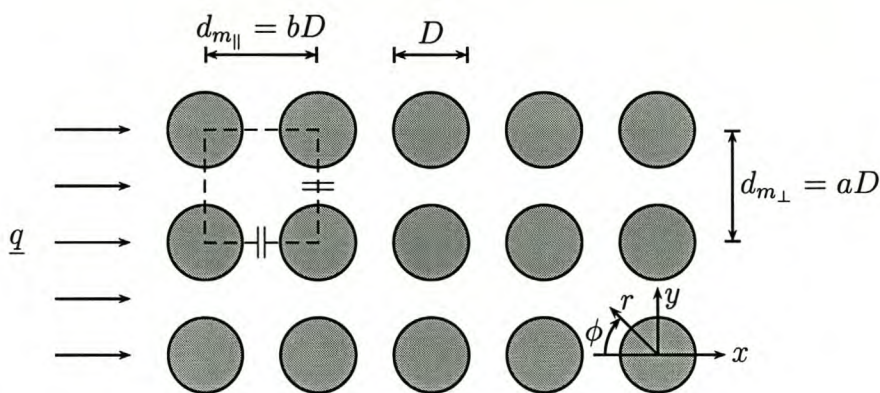


Figure 5.2: Illustration of a square array with the area inside the dashed line, showing the size of the smallest periodic volume.

The tubes of interest are smooth without any fins and the Reynolds numbers of experimental

data are available for the range: $3 \leq Re_{V_{max}D} \leq 2 \cdot 10^6$. Results for finned and/or inclined tubes are also included in the work of Zukauskas and Ulinskas, 1983, but fall outside the scope of the analysis in this chapter. The specific fluid used is Newtonian and when it is a gas the compressibility effects should be negligible at the high end of the Reynolds number range of the analysis. The geometries of both staggered and square arrays are described by the dimensionless parameters:

$$a \equiv \frac{d_{m\perp}}{D} \quad \text{and} \quad b \equiv \frac{d_{m\parallel}}{D}, \quad (5.1)$$

where the dimensions $d_{m\perp}$, $d_{m\parallel}$ and D are defined for both cases in Figures 5.1 and 5.2. The maximum average inter tube speed, V_{max} , can be expressed in terms of a as:

$$V_{max} = \frac{a}{a-1}q \quad ; \quad a \leq 2b^2 - 0.5. \quad (5.2)$$

For fully staggered tube banks, this critical speed may occur in the diagonal spacing between the tubes. When the spacing becomes smaller than $\frac{1}{2}(d_{m\perp} - D)$, V_{max} is given by:

$$V_{max} = \frac{a}{2\sqrt{\frac{a^2}{4} + b^2} - 2}q \quad ; \quad a > 2b^2 - 0.5. \quad (5.3)$$

Both Equations 5.2 and 5.3 are obtained by using the geometry as given in Figures 5.1 and 5.2. The speed, V_{max} , used here between the tubes should not be confused with u or w used in a RUC as they usually possess different values.

5.1 Cross-flow Forces on a Tube in a Bank

The pressure loss across a tube in a bank is a direct result of skin friction and/or form drag. At low Reynolds numbers, skin friction is the major contributing factor to the total flow resistance force \mathcal{F}_{\parallel} . At intermediate Reynolds numbers, form drag is predominant to such an extent that skin friction is negligible. Zukauskas and Ulinskas, 1983, states that the skin

friction at high Reynolds numbers ($Re_{V_{max}D} > 2 \times 10^5$) typically contributes 0.5-2% of $\mathcal{F}_{||}$. The skin friction is defined by Zukauskas and Ulinskas, 1983, as:

$$c_f \equiv \frac{2\tau_{S_{fs||}}}{\rho V_{max}^2}, \quad (5.4)$$

where $\tau_{S_{fs||}}$ is the mean streamwise component of the shear stress on the tube surface. The local shear stress is given by

$$\tau_{S_{fs}} = \mu \left(\frac{\partial v}{\partial r} \right)_{S_{fs}}, \quad (5.5)$$

where μ is the dynamic viscosity and $\left(\frac{\partial v}{\partial r} \right)_{S_{fs}}$ is the tangential speed gradient at and normal to the tube wall (see Figures 5.1 and 5.2). The mean streamwise shear stress can now be calculated as

$$\tau_{S_{fs||}} = \frac{2}{\pi D} \int_{\phi=0}^{\phi=\pi} \tau_{S_{fs}} r \cos \phi \, d\phi, \quad (5.6)$$

where $\tau_{S_{fs}} = 0$ in the regions of recirculation. The variables ϕ and r are defined in Figures 5.1 and 5.2 for both bank configurations. To solve the integral in Equation 5.6, it is necessary to know the point of flow impact and the point of separation as it is only between these points that a significant speed gradient exists, contributing to the skin friction. The rest of the cylinder is only subjected to local flow recirculation which is turbulent at high Reynolds numbers. For fully staggered tube banks, Zukauskas and Ulinskas, 1983, took the point of impact as $\phi = 0^\circ$ (assumed for the range $2 \leq Re_{V_{max}D} \leq 10^5$) and for square array banks it was determined from the experimental data with Figure 5.3 as result. Zukauskas and Ulinskas, 1983, defined the separation point where $\left(\frac{\partial u}{\partial r} \right)_{S_{fs}} = 0$ as the flow passes around the cylinder and breaks away from the wall. However, an indication of the angle at which flow separation occurs is not given.

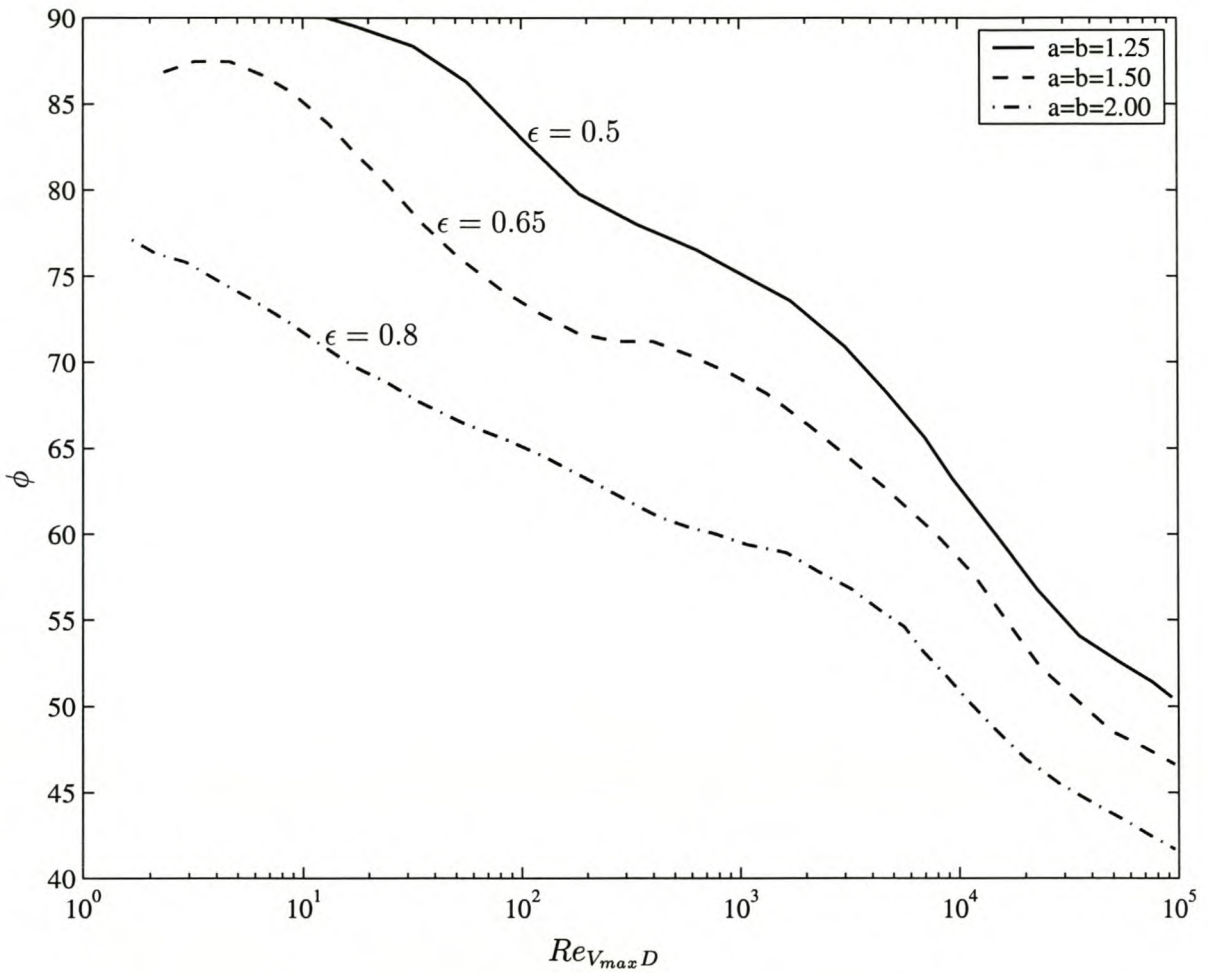


Figure 5.3: The point of impact on a cylinder in a square array tube bank as determined from the experimental data of Zukauskas and Ulinskas, 1983.

The angle of flow separation is estimated from the results of White, 1994, for a single cylinder. With non-separating flow at very low Reynolds numbers, typically $Re_{qD} < 10$, the separating point can be estimated to be at $\phi = 180^\circ$. At flow rates higher than $Re_{qD} = 10$, the flow separates from the cylinder in the region of $\phi = 120^\circ$ up to $Re_{qD} = 10^4$. Increasing the flow to $10^4 < Re_{qD} < 3 \times 10^5$ causes it to separate at a smaller angle of approximately $\phi = 82^\circ$. Above $Re_{qD} < 3 \times 10^5$, the recirculation zone becomes turbulent and the separation angle increases again to $\phi = 120^\circ$ or, according to Zukauskas and Ulinskas, 1983, $\phi = 140^\circ$. The angles given for ϕ are not easy to determine and should be used as a guidelines only. This does not apply to other shapes where the presence of edges has a great influence on

the point of separation of the solid. It is more likely to be situated at an edge for low to intermediate Reynolds numbers.

When form drag dominates at intermediate Reynolds numbers (Forchheimer range), a drag coefficient, C_D is used to relate the fluidal drag force on the tube with the Reynolds number. Zukauskas and Ulinskas, 1983, defines the drag force as

$$\mathcal{F}_{\parallel} \equiv C_D \frac{1}{2} \rho V_{max}^2 A_{\perp}, \quad (5.7)$$

where $A_{\perp} = DL_{tube}$ is the projected area of a tube perpendicular to the streamwise direction and V_{max} the reference speed. For a single object the reference speed is that of the free stream. It should be noted that the skin friction may be included with the form drag in the factor C_D , to provide a single factor to be applicable to the low and intermediate Reynolds number range. The values for C_D used in this document include both these effects. A practical method to determine \mathcal{F}_{\parallel} is to measure the surface pressure of a tube at a number, n_0 , of uniformly distributed points on the circumference and solve the following summation given by Zukauskas and Ulinskas, 1983:

$$\mathcal{F}_{\parallel} = \frac{\pi DL_{tube}}{n_0} \sum_{i=1}^{n_0} P_{\phi_i} \cos \phi_i. \quad (5.8)$$

Another possibility to determine the force, \mathcal{F}_{\parallel} , is to measure it directly at the tube mounting points, but this may be an arduous task.

The significance of the point of impact and separation point differences between flow past round and rectangular bodies is that their effects manifest in the drag coefficient. The flow regions as given above can be identified clearly from the drag coefficient of a single cylinder, shown in Figure 5.4. This coefficient is used for the RUC modelling later in this chapter and a decision has to be made whether to use the porous media solid matrix as basis for C_D or that of the rectangular solid of the RUC. For the purpose of this study, to include as many significant flow effects as possible, the drag coefficient of a cylinder will be used in the RUC model for tube banks.

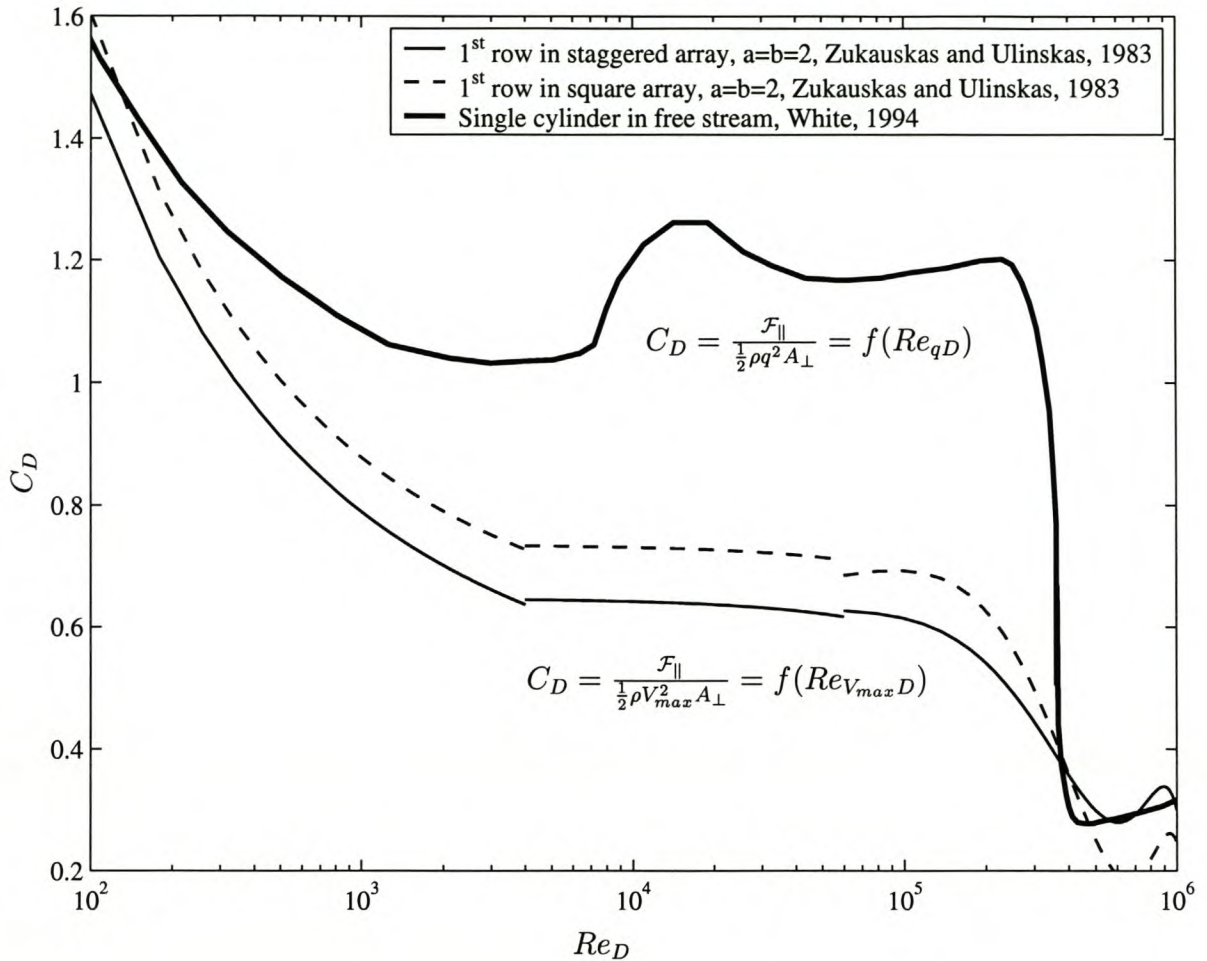


Figure 5.4: Drag coefficient on a smooth tube in a bank as by Equation sets 5.9 and 5.10 with $a = b = 2$. For convenience, the drag coefficient of a single cylinder in the free stream is given and is comparable with the other drag coefficient given when V_{max} at a tube in a bank is assumed to be the equivalent of q around a cylinder in a free stream. C_D is based on the tube frontal area, $A_{\perp} = DL$. Note that the characteristic speed on which the Re number is based, is different between plots as evident from expressions associated with each.

5.2 Pressure Loss Across a Bank of Tubes

The presence of neighbouring solid elements around a single body subjected to flow, results in a different drag coefficient to that of a single body in a free stream. This is also the case

for tubes in a tube bank as investigated in this section. The two subsections that follow briefly present equations fitted by Zukauskas and Ulinskas, 1983, to experimental flow data for staggered and square tube banks in cross-flow.

The drag coefficient of the first tube row in both staggered and square banks were experimentally determined by Zukauskas and Ulinskas, 1983, using Equations 5.8 and 5.7. Zukauskas and Ulinskas, 1983, fitted curves through the data to relate the C_D values of the first tube row in each case with the Reynolds number. The result for the first tube row in a staggered array is:

$$\begin{aligned}
 C_D &= 0.417 \exp\left(4.932 Re_{V_{max}D}^{-0.296}\right) && ; 10^2 < Re_{V_{max}D} < 4 \cdot 10^3 \\
 C_D &= 0.647 - 0.5 \cdot 10^{-6} Re_{V_{max}D} && ; 4 \cdot 10^3 < Re_{V_{max}D} < 6 \cdot 10^4 \\
 C_D &= 0.618 + 0.491 \cdot 10^{-6} Re_{V_{max}D} - 6.303 \cdot 10^{-12} Re_{V_{max}D}^2 \\
 &\quad + 10.694 \cdot 10^{-18} Re_{V_{max}D}^3 - 5.2 \cdot 10^{-24} Re_{V_{max}D}^4 && ; 6 \cdot 10^4 < Re_{V_{max}D} < 10^6 .
 \end{aligned} \tag{5.9}$$

For the square array the result for the first tube row is:

$$\begin{aligned}
 C_D &= 0.535 \exp\left(5.378 Re_{V_{max}D}^{-0.345}\right) && ; 10^2 < Re_{V_{max}D} < 4 \cdot 10^3 \\
 C_D &= 0.735 - 0.411 \cdot 10^{-6} Re_{V_{max}D} && ; 4 \cdot 10^3 < Re_{V_{max}D} < 6 \cdot 10^4 \\
 C_D &= 0.621 + 0.169 \cdot 10^{-5} Re_{V_{max}D} - 11.343 \cdot 10^{-12} Re_{V_{max}D}^2 \\
 &\quad + 16.656 \cdot 10^{-18} Re_{V_{max}D}^3 - 7.377 \cdot 10^{-24} Re_{V_{max}D}^4 && ; 6 \cdot 10^4 < Re_{V_{max}D} < 10^6 .
 \end{aligned} \tag{5.10}$$

Equation sets 5.9 and 5.10 are plotted in Figure 5.4. It is interesting to note that the drag forces on the first tube row in a square array are generally higher than those of a staggered array. For comparison, the drag on a cylinder in a free stream is also included in Figure 5.4. This comparison is only possible if one assumes that the free stream speed for a single cylinder is more or less the same as the maximum average speed at a tube in a bank.

Figure 5.4 gives some insight into what happens between the tubes in the bank. Firstly, the drag of the cylinders in the bank is less at the intermediate Reynolds numbers, possibly because the recirculation region behind each cylinder is much smaller than in the free stream case. At intermediate Reynolds numbers there is also the sharp increase in C_D at $Re_{qD} \approx 10^4$

for the single cylinder. This is most probably due to the separation points which are, to a large degree, forced to be at a fixed position for each cylinder in a bank causing the recirculation zone to be invariant in the intermediate Reynolds number range. Another point is that C_D for the second row and onwards should be even less than that of the first row in a square array, as the cylinders are partially in the recirculation zone of a cylinder in the upstream direction. If this were not the case, it would have been impossible to obtain the data represented in Figure 5.4. Zukauskas and Ulinskas, 1983, also give some experimental results specifically to illustrate this drag difference between the first tube row and those downstream.

The microscopic effects of the flow through a tube bank as described above all contribute to the overall pressure loss across it. Using the symbols in Figures 5.1 and 5.2 and taking the number of tube rows as k , the pressure loss according to Zukauskas and Ulinskas, 1983, is given by

$$\Delta P = f(V_{max}, d_{m\perp}, d_{m\parallel}, D, k, \mu, \rho). \quad (5.11)$$

The experimental results that Zukauskas and Ulinskas, 1983, obtained from various sources are represented by the equation sets that follow in the next two subsections. They relate the flow characteristics, represented by the Euler number, in terms of the Reynolds number. The curves, as fitted by Zukauskas and Ulinskas, 1983, only apply piecewise and the transition between subsequent intervals are not smooth as expected. Nevertheless, the equations still give a good approximation of the relevant data. The Euler number used for tube banks as defined by Zukauskas and Ulinskas, 1983, is

$$Eu \equiv \frac{2\Delta P_{bank}}{\rho V_{max}^2 k}. \quad (5.12)$$

This factor is closely related to the Fanning friction factor as defined in Equation 4.27.

Staggered Array

A range of empirical expressions for the Euler number is given by Zukauskas and Ulinskas, 1983, for an equilateral staggered array with the notation as given in Figure 5.1 where $a = \frac{2}{\sqrt{3}}b$. A correction factor (k_1) is used by Zukauskas and Ulinskas, 1983, to cater for other configurations determined by the ration $a : b$. Both the staggered and square array cases in this thesis use configurations where $k_1 = 1$, thus it can be discarded of as done in the rest of this chapter. The expressions are as follows:

Case 1: $a = 1.25$; $\epsilon = 0.420$

For the range $3 < Re_{V_{max}D} < 10^3$:

$$Eu = 0.795 + \frac{0.247 \cdot 10^3}{Re_{V_{max}D}} + \frac{0.335 \cdot 10^3}{Re_{V_{max}D}^2} - \frac{0.155 \cdot 10^4}{Re_{V_{max}D}^3} + \frac{0.421 \cdot 10^4}{Re_{V_{max}D}^4}. \quad (5.13)$$

For the range $10^3 < Re < 2 \cdot 10^6$:

$$Eu = 0.245 + \frac{0.339 \cdot 10^4}{Re_{V_{max}D}} - \frac{0.984 \cdot 10^7}{Re_{V_{max}D}^2} + \frac{0.132 \cdot 10^{11}}{Re_{V_{max}D}^3} - \frac{0.599 \cdot 10^{13}}{Re_{V_{max}D}^4}. \quad (5.14)$$

Case 2: $a = 1.5$; $\epsilon = 0.597$

For the range $3 < Re_{V_{max}D} < 10^3$:

$$Eu = 0.683 + \frac{0.111 \cdot 10^3}{Re_{V_{max}D}} - \frac{0.973 \cdot 10^2}{Re_{V_{max}D}^2} + \frac{0.426 \cdot 10^3}{Re_{V_{max}D}^3} - \frac{0.574 \cdot 10^3}{Re_{V_{max}D}^4}. \quad (5.15)$$

For the range $10^3 < Re_{V_{max}D} < 2 \cdot 10^6$:

$$Eu = 0.203 + \frac{0.248 \cdot 10^4}{Re_{V_{max}D}} - \frac{0.758 \cdot 10^7}{Re_{V_{max}D}^2} + \frac{0.104 \cdot 10^{11}}{Re_{V_{max}D}^3} - \frac{0.482 \cdot 10^{13}}{Re_{V_{max}D}^4}. \quad (5.16)$$

Case 3: $a = 2.0$; $\epsilon = 0.773$

For the range $7 < Re_{V_{max}D} < 10^2$:

$$Eu = 0.713 + \frac{0.448 \cdot 10^2}{Re_{V_{max}D}} - \frac{0.126 \cdot 10^3}{Re_{V_{max}D}^2} - \frac{0.582 \cdot 10^3}{Re_{V_{max}D}^3}. \quad (5.17)$$

For the range $10^2 < Re_{V_{max}D} < 10^4$:

$$Eu = 0.343 + \frac{0.303 \cdot 10^3}{Re_{V_{max}D}} - \frac{0.717 \cdot 10^5}{Re_{V_{max}D}^2} + \frac{0.880 \cdot 10^7}{Re_{V_{max}D}^3} - \frac{0.380 \cdot 10^9}{Re_{V_{max}D}^4}. \quad (5.18)$$

For the range $10^4 < Re_{V_{max}D} < 2 \cdot 10^6$:

$$Eu = 0.162 + \frac{0.181 \cdot 10^4}{Re_{V_{max}D}} + \frac{0.792 \cdot 10^8}{Re_{V_{max}D}^2} - \frac{0.165 \cdot 10^{13}}{Re_{V_{max}D}^3} + \frac{0.872 \cdot 10^{16}}{Re_{V_{max}D}^4}. \quad (5.19)$$

Case 4: $a = 2.5$; $\epsilon = 0.855$

For the range $10^2 < Re_{V_{max}D} < 5 \cdot 10^3$:

$$Eu = 0.330 + \frac{0.989 \cdot 10^2}{Re_{V_{max}D}} - \frac{0.148 \cdot 10^5}{Re_{V_{max}D}^2} + \frac{0.192 \cdot 10^7}{Re_{V_{max}D}^3} - \frac{0.862 \cdot 10^8}{Re_{V_{max}D}^4}. \quad (5.20)$$

For the range $5 \cdot 10^3 < Re_{V_{max}D} < 2 \cdot 10^6$:

$$Eu = 0.119 + \frac{0.498 \cdot 10^4}{Re_{V_{max}D}} - \frac{0.507 \cdot 10^8}{Re_{V_{max}D}^2} + \frac{0.251 \cdot 10^{12}}{Re_{V_{max}D}^3} - \frac{0.463 \cdot 10^{15}}{Re_{V_{max}D}^4}. \quad (5.21)$$

These results are plotted in Figure 5.5 and compared with the RUC model as in Equation 5.35.

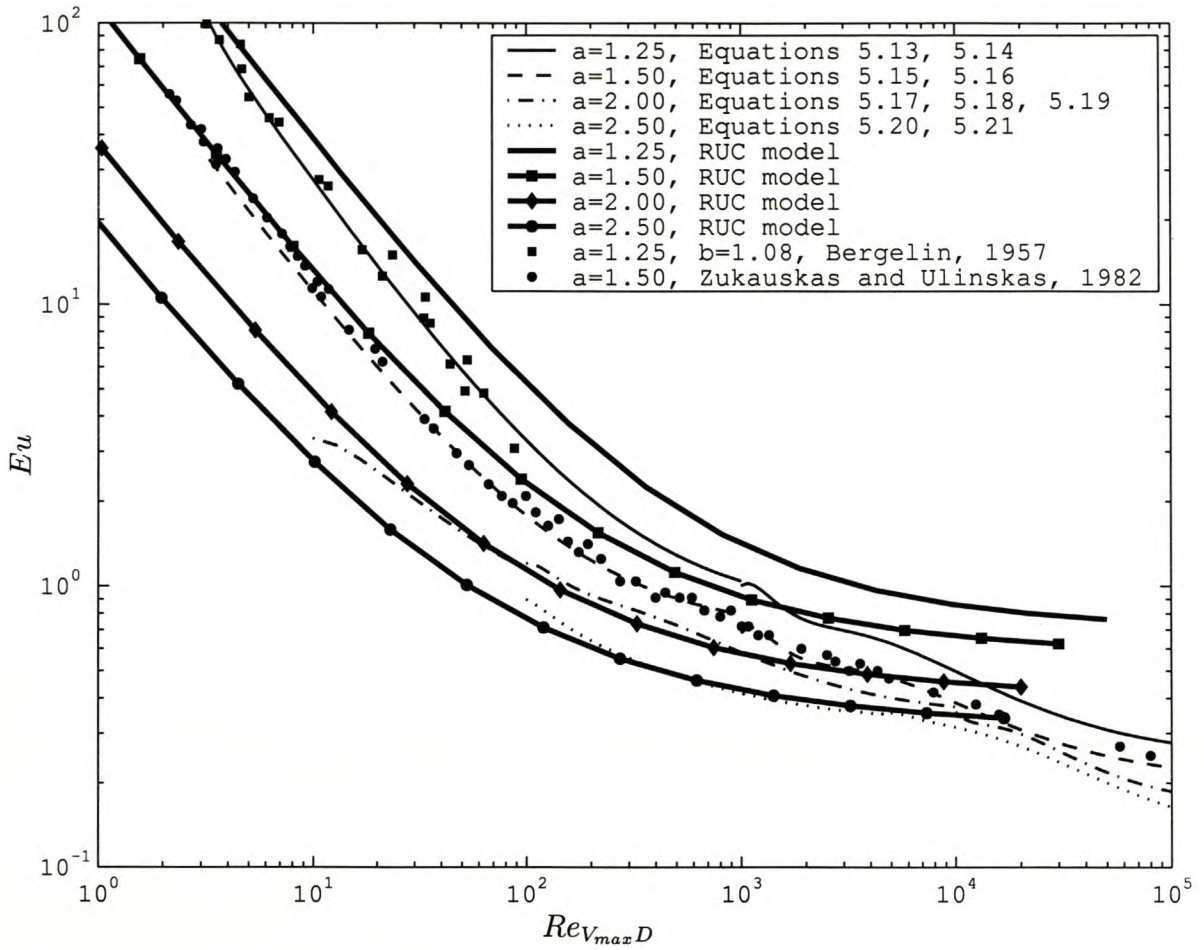


Figure 5.5: Pressure drop across a staggered tube bank. Equations 5.13 to 5.21 and the RUC model (Equation 5.35) results are displayed.

Square Array

The following empirical expressions are given by Zukauskas and Ulinskas, 1983, for the square array where $a = b$.

Case 1: $a = 1.25$; $\epsilon = 0.497$

For the range $3 < Re_{V_{max}D} < 2 \cdot 10^3$:

$$Eu = 0.272 + \frac{0.207 \cdot 10^3}{Re_{V_{max}D}} + \frac{0.102 \cdot 10^3}{Re_{V_{max}D}^2} - \frac{0.286 \cdot 10^3}{Re_{V_{max}D}^3}. \quad (5.22)$$

For the range $2 \cdot 10^3 < Re_{umaxD} < 2 \cdot 10^6$

$$Eu = 0.267 + \frac{0.249 \cdot 10^4}{Re_{VmaxD}} - \frac{0.927 \cdot 10^7}{Re_{VmaxD}^2} + \frac{0.100 \cdot 10^{11}}{Re_{VmaxD}^3}. \quad (5.23)$$

Case 2: $a = 1.5$; $\epsilon = 0.651$

For the range $3 < Re_{VmaxD} < 2 \cdot 10^3$:

$$Eu = 0.263 + \frac{0.867 \cdot 10^2}{Re_{VmaxD}} - \frac{0.202 \cdot 10^1}{Re_{VmaxD}^2}. \quad (5.24)$$

For the range $2 \cdot 10^3 < Re_{VmaxD} < 2 \cdot 10^6$:

$$Eu = 0.235 + \frac{0.197 \cdot 10^4}{Re_{VmaxD}} - \frac{0.124 \cdot 10^8}{Re_{VmaxD}^2} + \frac{0.312 \cdot 10^{11}}{Re_{VmaxD}^3} - \frac{0.274 \cdot 10^{14}}{Re_{VmaxD}^4}. \quad (5.25)$$

Case 3: $a = 2.0$; $\epsilon = 0.804$

For the range $7 < Re_{VmaxD} < 800$:

$$Eu = 0.188 + \frac{0.566 \cdot 10^2}{Re_{VmaxD}} - \frac{0.646 \cdot 10^3}{Re_{VmaxD}^2} + \frac{0.601 \cdot 10^4}{Re_{VmaxD}^3} - \frac{0.183 \cdot 10^5}{Re_{VmaxD}^4}. \quad (5.26)$$

For the range $800 < Re_{VmaxD} < 2 \cdot 10^6$:

$$Eu = 0.247 - \frac{0.595 Re_{VmaxD}}{10^6} + \frac{0.150 Re_{VmaxD}^2}{10^{11}} - \frac{0.137 Re_{VmaxD}^3}{10^{17}} + \frac{0.396 Re_{VmaxD}^4}{10^{24}}. \quad (5.27)$$

Case 4: $a = 2.5$; $\epsilon = 0.874$

For the range $600 < Re_{VmaxD} < 2 \cdot 10^5$:

$$Eu = 0.177 - 0.311 \cdot 10^{-6} Re_{VmaxD} + 0.117 \cdot 10^{-11} Re_{VmaxD}^2. \quad (5.28)$$

The results of the square tube banks above are plotted in Figure 5.6 and compared with the RUC model as in Equation 5.35.

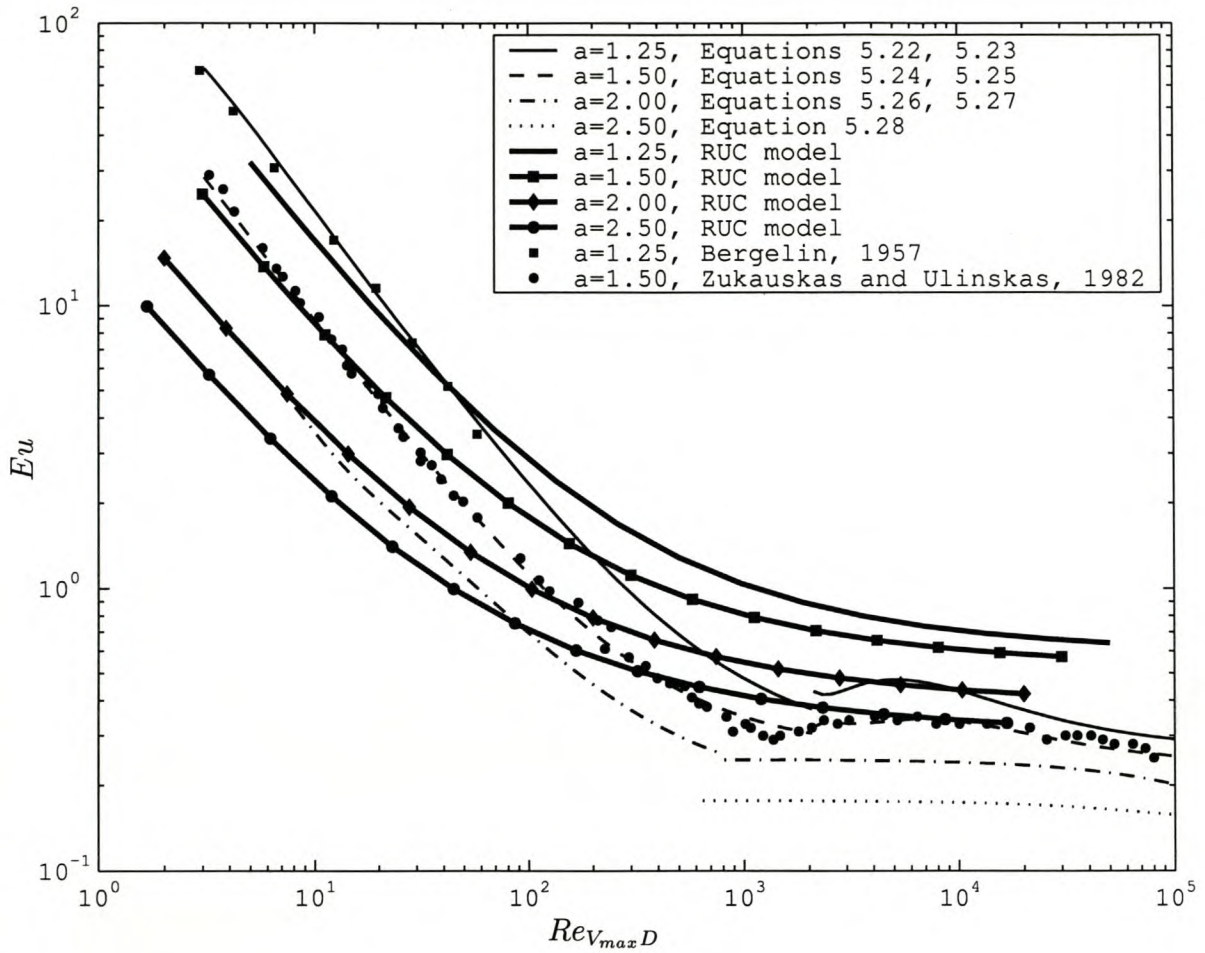


Figure 5.6: Pressure drop across a square tube bank. Equations 5.22 to 5.28 and the RUC model (Equation 5.35) results are displayed.

5.3 Tube Bank Modelled with a RUC

The RUC model as derived in Chapter 4 is now used to estimate the pressure loss across the tube banks of Section 5.2. Firstly, the staggered case is considered, after which the square array follows. The drag coefficient for a single circular cylinder in a cross flow is obtained from White, 1994, which includes both the skin friction and pressure drag.

In order to evaluate Equations 4.32 to 4.34, it is necessary to know the RUC specific variables

(e.g. β , ϵ , χ and U_o) in terms of the parameters for a tube bank. The size and aspect ratio of the RUC is in this case determined by the smallest rectangular building block for the tube banks as shown in Figures 5.1 and 5.2 with dashed lines. A tube is to be modelled with a square cylinder as the solid in the RUC. To obey the rule of equal porosities in Section 4.1, the cross sectional area of a tube is to be equal to that of a square cylinder. With this taken into account, the RUC specific variables with reference to Figure 4.1 are:

$$d_{\perp} = aD \quad \text{and} \quad d_{\parallel} = bD \quad (5.29)$$

$$d_{s_{\parallel}} = d_{s_{\perp}} = \frac{\sqrt{\pi}}{2} D \quad (5.30)$$

$$\beta = \frac{2a - \sqrt{\pi}}{2b - \sqrt{\pi}} \quad (5.31)$$

$$\epsilon = 1 - \frac{\pi}{4ab} \quad (5.32)$$

$$\chi = \frac{4ab - \pi}{2b(2a - \sqrt{\pi})} \quad (5.33)$$

$$U_o = abD^2 z. \quad (5.34)$$

With D as the characteristic dimension and expressing the RUC dimensions in terms of a and b in Equation 4.33, the following result is obtained:

$$\begin{aligned} FD^2 &= \frac{12\chi z D^2}{\epsilon U_o} \left(\frac{d_{s_{\parallel}}}{d_{p_{\perp}}} + \beta \frac{d_{s_{\perp}}}{d_{p_{\parallel}}} \right) + \frac{\chi^2 C_D z D^2 Re_{qD}}{2\epsilon^2 U_o} \\ &= \frac{12\chi z D^2}{\epsilon U_o} \left(\frac{\sqrt{\pi}}{2a - \sqrt{\pi}} + \beta \frac{\sqrt{\pi}}{2b - \sqrt{\pi}} \right) + \frac{\sqrt{\pi} \chi^2 C_D z D^2 Re_{qD}}{4\epsilon^2 U_o}. \end{aligned} \quad (5.35)$$

The value(s) used for C_D can be a constant or a function of the Reynolds number. The graph in White, 1994, of C_D vs. Re_{qD} for a cylinder was digitized for the range $0.1 < Re_{qD} < 10^4$ and a third degree polynomial fitted through the logarithmic data yielding

$$C_D = 10^{[c_1 + c_2 \log(Re_{qD}) + c_3 \log(Re_{qD})^2 + c_4 \log(Re_{qD})^3]}, \quad \text{where} \quad \begin{aligned} c_1 &= 0.9645 \\ c_2 &= -0.6128 \\ c_3 &= 0.1314 \\ c_4 &= -0.01 \end{aligned} \quad (5.36)$$

There is no significant deviation of Equation 5.36 from the original curve of White, 1994, within the given range and is therefore suitable to use in Equation 5.35.

If C_D is to be taken as constant, the recommended value to use is $C_D = 1.1$ for the range $10^3 < Re_{qD} < 10^4$ and $C_D = 1.2$ for the range $10^4 < Re_{qD} < 10^5$. Above $Re_{qD} = 10^5$, the flow becomes turbulent and C_D falls to about 0.3. These drag coefficient ranges can be visually identified in Figure 5.4 on the drag curve of a single cylinder, obtained from White, 1994.

The result of the values $C_D = 1.1$ and $C_D = f(Re_{qD})$ used in Equation 5.35 are displayed in Figure 5.7 for comparison. The individual contribution of both the Darcy and Forchheimer terms are also given in each case. The dashed line represents the Forchheimer term's contribution where C_D is obtained from Equation 5.36 and the dash-dot line if $C_D = 1.1$. The difference between the two Forchheimer terms is clearly visible below $Re_{qD} = 10^3$, which is expected as the constant value is only applicable above $Re_{qD} = 10^3$.

The question can now be asked if the viscous effects are accounted for twice in Equation 5.35 when $C_D = f(Re_{qD})$ is used as it included in both the Darcy term and C_D . To clarify this, it is useful to examine the contribution of each term to the tube bank resistance in Figure 5.7. The constant value of the Darcy term is approximately at $FD^2 = 54$ and the Forchheimer term with $C_D = f(Re_{qD})$ should strive to the same value at low Reynolds numbers. This is not the case and the most probable reason is that C_D is only valid for a single cylinder in a free stream and it is assumed to apply directly to the RUC theory. Should only the Forchheimer term with $C_D = f(Re_{qD})$ be used to determine FD^2 , the values at the lower end of the Re_{qD} range would be too low. If this on the other hand is used in conjunction with the Darcy term, the apparent error would be higher, as shown in Figure 5.7, to a maximum of 40%.

As already mentioned in Section 5.1, another phenomenon that plays a role is that with spheres and tubes, including elliptic forms, the flow separation point is not stationary. The effect this has on the interstitial flow in a porous medium at moderate to high Reynolds numbers may be significant when compared to angular shapes.

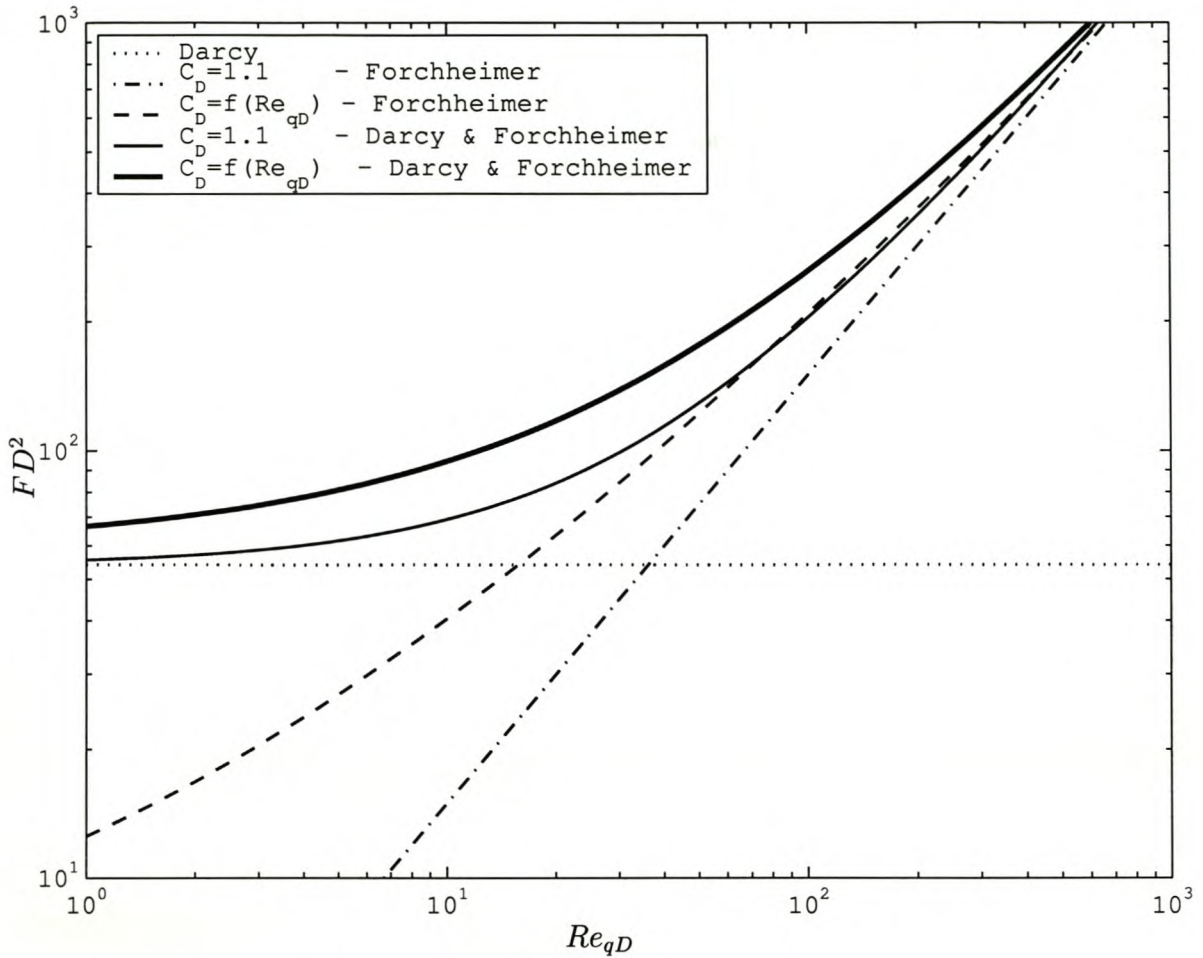


Figure 5.7: The two terms of Equation 5.35 are used to illustrate the difference between using a constant drag coefficient and one that is based on the Reynolds number. $C_D \approx 1.1$ for $Re_{qD} = 1000$ and $C_D = f(Re_{qD})$ is obtained from Equation 5.36.

5.4 Comparison of Experimental Data with Results of the RUC Model

In this section the RUC solution of Equation 5.35 is evaluated against the tube bank data published in Zukauskas and Ulinskas, 1983, and Bergelin, 1950. To facilitate the comparison of results from Zukauskas and Ulinskas, 1983, and the RUC theory, it is necessary to plot the data on the same axes.

Using the matrix size relative to fibre diameter as defined in Equation 5.1 and the number of tube columns in the bank, k , the pressure gradient in terms of variables as used by Zukauskas and Ulinskas, 1983, is

$$-\frac{dP}{dx} = \frac{\Delta P_{bank}}{bDk}. \quad (5.37)$$

The speed in the Reynolds number used by Zukauskas and Ulinskas, 1983, ($Re_{V_{max}D}$), which is based on the maximum average speed present between a pair of tubes, is different from that used in the RUC theory which is based on the seepage speed, q . The two Reynolds numbers are related by

$$Re_{V_{max}D} = \frac{a}{a-1} Re_{qD}, \quad (5.38)$$

where V_{max} was obtained from Equation 5.2. For other tube configurations, Equation 5.3 may apply instead, in which case the equation above should be changed accordingly. By using Equations 5.2 and 5.12, the pressure gradient, $-\frac{dp}{dx}$, in terms of the Euler number and the seepage speed is

$$-\frac{dP}{dx} = \frac{a^2}{2b(a-1)^2} \frac{\rho q^2}{D} Eu. \quad (5.39)$$

It now follows that the friction factor for porous media can be expressed as

$$F = -\frac{\epsilon}{\mu q} \frac{dP}{dx} = \frac{a^2}{2b(a-1)^2} \frac{\epsilon \rho q}{\mu D} Eu. \quad (5.40)$$

A convenient dimensionless form of Equation 5.40 is

$$FD^2 = \frac{a^2}{2b(a-1)^2} \epsilon Re_{qD} Eu. \quad (5.41)$$

Equations 5.37 to 5.41 and 5.2 are necessary to plot the data according to the variables used in the RUC model. These are also valid for both staggered ($a = \frac{2}{\sqrt{3}}b$) and square ($a = b$) cases.

Figures 5.8 and 5.9 display the comparison of the results obtained from Zukauskas and Ulinskas, 1983, and the RUC theory. It should be noted that the RUC model for both staggered and square cases are exactly the same with the only difference being the ratio $a : b$. From Figures 5.8 and 5.9 it can be concluded that the RUC model results are better for staggered than for square arrays. The same should hold for the case where the tubes are randomly positioned, as the microscopic flow channels are also not straight.

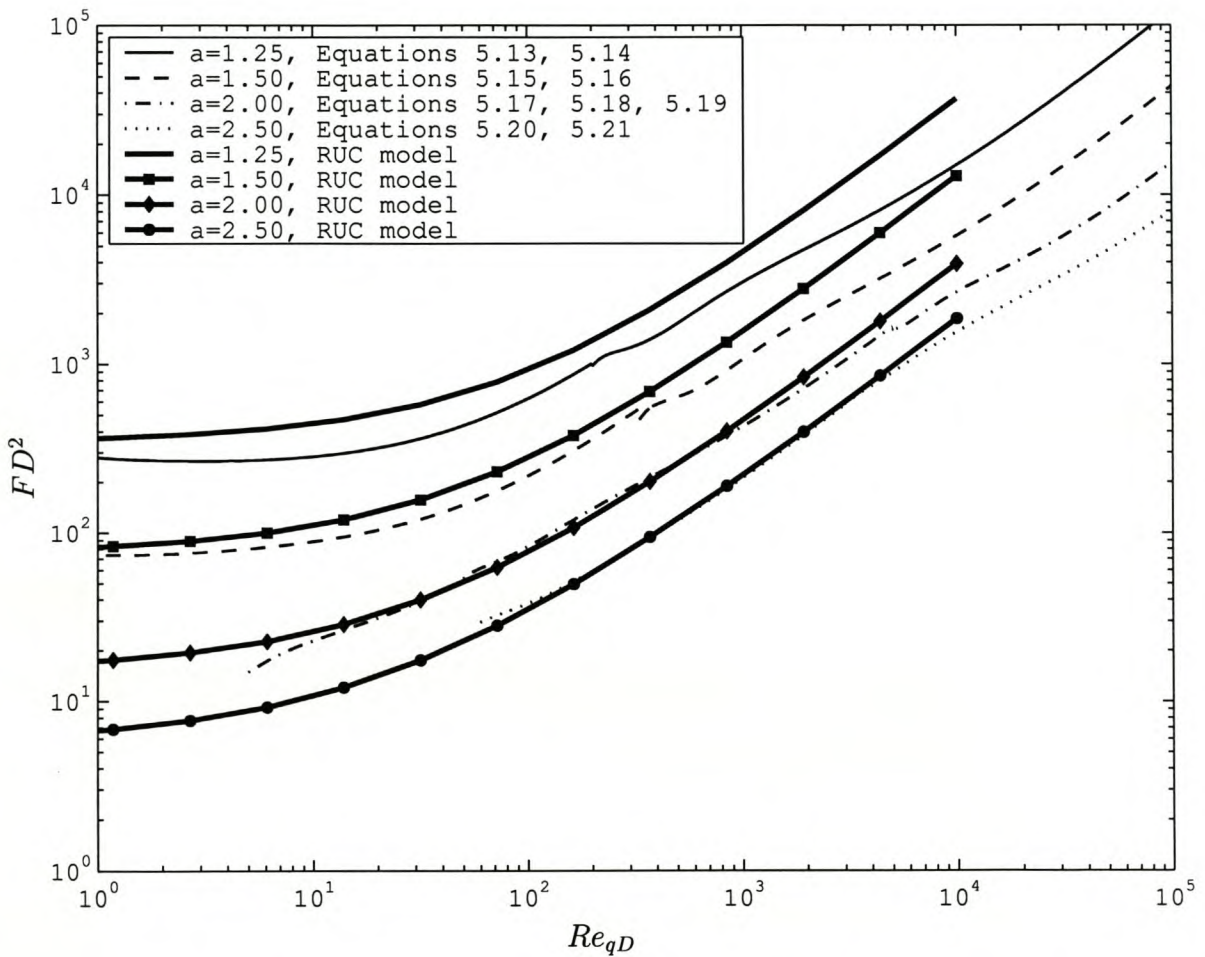


Figure 5.8: The porous media friction factor for a staggered tube bank. Experimental results of Zukauskas and Ulinskas, 1983, are compared with the RUC model (Equation 5.35).

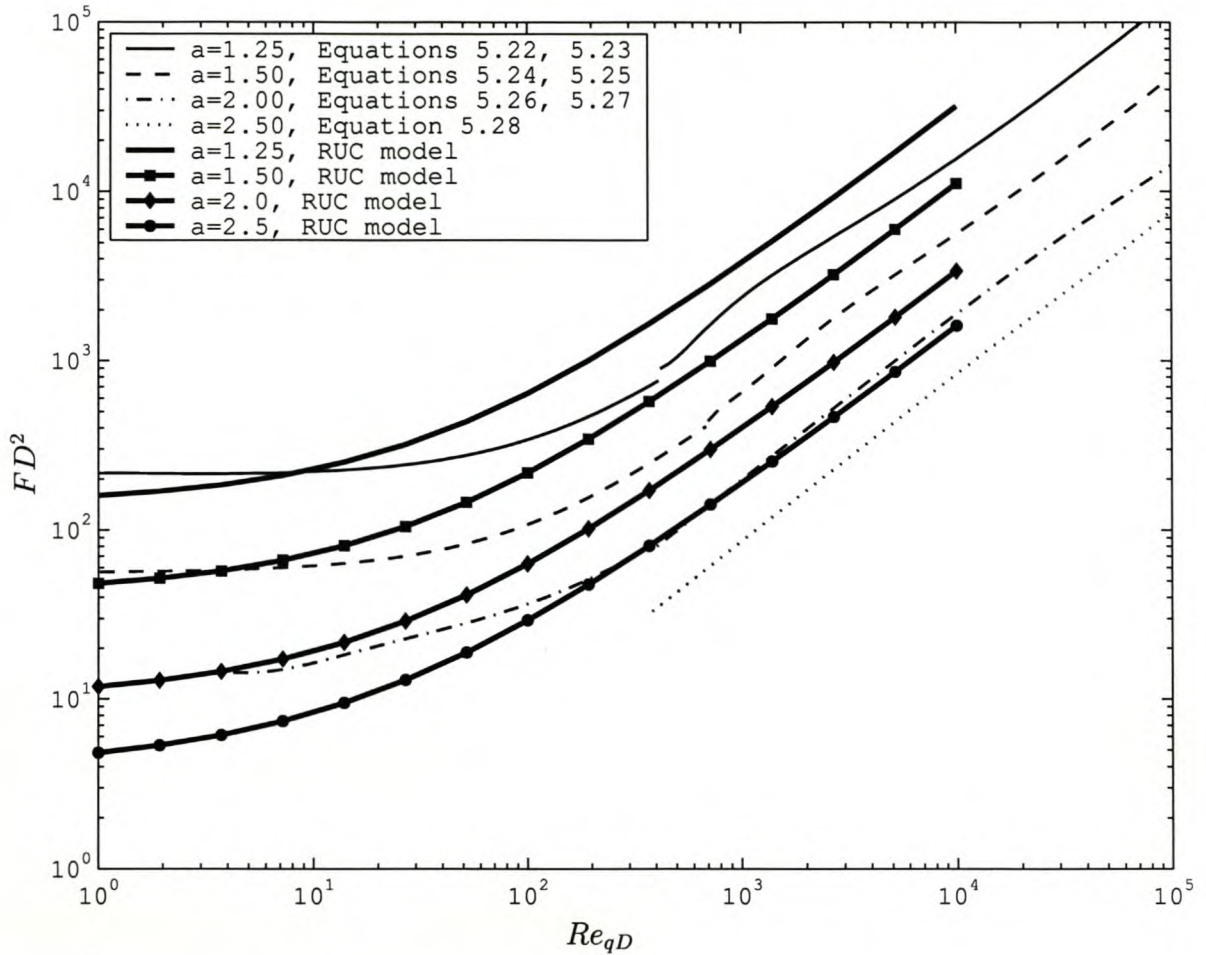


Figure 5.9: The porous media friction factor for a square array tube bank. Experimental results of Zukauskas and Ulinskas, 1983, are compared with the RUC model (Equation 5.35).

It is now questioned whether the RUC model can be compared to experimental data obtained from a model which is not geometrically exactly the same, because appropriate data are not always readily available. In an equilateral staggered tube bank, $a = \frac{2}{\sqrt{3}}b$, tube rows are about 13% closer to each other than in the streamwise direction of the case where $a = b$. The effect of this difference on the permeability of a bank should be negligible, because the critical flow passage area, where V_{max} is calculated, is usually between the tubes perpendicular to the streamwise direction. Therefore, the fact that the row downstream is a bit closer in the case of the equilateral array does not significantly affect the frictional resistance through the bank for small changes. This is briefly discussed by Zukauskas, 1987, where the analysis is

always based upon the minimum inter-tube spacing through which the flow is forced.

Some of the data of Zukauskas, 1987, and Bergelin, 1950, are also given in Figures 5.5 and 5.6 to show that the curve fits of Zukauskas and Ulinskas, 1983, are indeed fairly accurate, although there are inconsistencies at the transitions between the curves for each bank configuration. It also shows that for the staggered array, there is not a significant difference between equilateral and $a = b$ bank configurations.

A few aspects regarding the shortcomings of the RUC model are pointed out. Firstly the specific RUC solution in Equations 4.32 to 4.34 can play a significant role. However, those that are not used give inaccurate results as shown in Chapter 6. Another point is that the tubes are far apart (high porosity), resulting in fluid flow which is not channelled between parallel surfaces as assumed in the RUC theory. In a staggered array, the flow pattern is much closer to a randomly set up bank than a square bank, where flow is normally channelled between rows. This is why the RUC model results for a staggered array are considerably more realistic.

Chapter 6

Flow Through a Stack in a Timber-drying Kiln

A timber-drying kiln is used for drying timber boards cut from logs in order to make it usable for the furniture and construction industries. Considerable risks are involved during the drying process and it is therefore important to examine each aspect of this process. It is also economically favourable to design a timber-drying kiln such that operating costs are kept to a minimum. Both the aspects of cost and risk receive attention in this chapter, where the two-dimensional porous media flow model is applied to a timber stack inside a timber-drying kiln during drying.

The drying process in modern kilns relies on computer controlled drying schedules, which regulate the air temperature, moisture content and flow direction. With these three variables under control, the success of such a schedule is still dependent on what is happening around and inside a stack regarding the airflow. In this investigation the airflow to and from the stack is assumed to be uniform, as this is a pre-requisite for a well-designed kiln. The basic layout of a timber-drying kiln is shown in Figure 6.1 containing a timber stack which is usually 2.2 *m* wide, 3 *m* high and 6 – 7 *m* long. Various other kiln configurations are used around the world, of which the majority is described by Koehler and Thelen, 1926. Although the latter book is not a recent publication, the fundamentals of the timber industry have not changed. The main components of a stack are the wheelbase, boards to be dried and the

spacers, with the latter commonly known as stickers in the timber industry. The stickers, which form a critical component of a stack, create the passages to facilitate the airflow between the boards as shown in Figure 6.1.

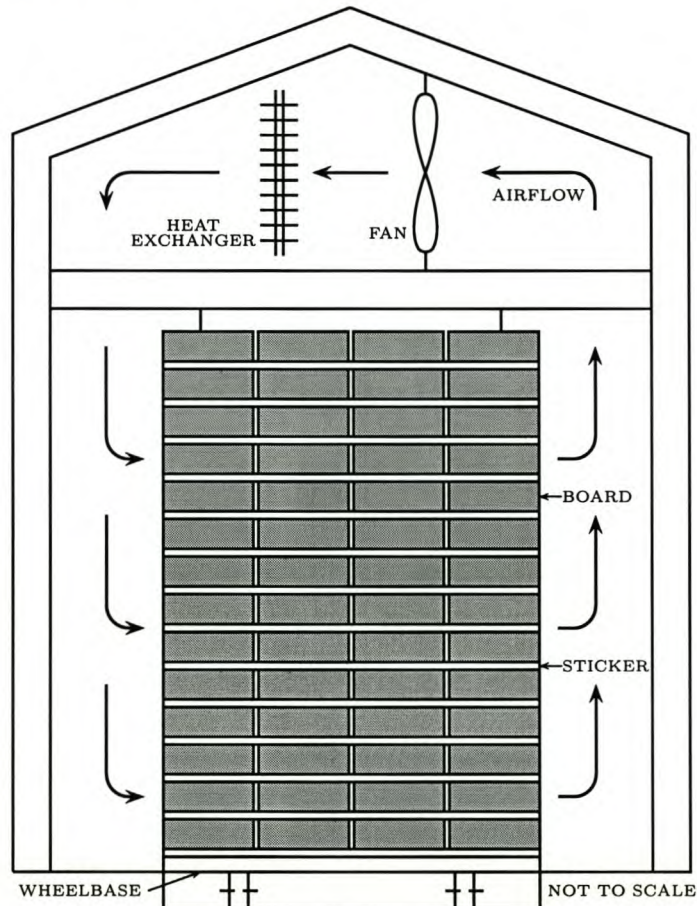


Figure 6.1: A section through a typical timber-drying kiln with stack in the centre.

The energy requirements in a kiln are both thermal and mechanical. The first is heat, which is obtained by burning the sawdust and chips from the sawmill in a steam heating system. The second is electricity for the air fans operated by a control system according to a preset drying schedule. The purpose of the airflow in a timber-drying kiln is to convey air at a specified temperature, relative humidity and velocity through the stacks. When optimizing a kiln design it is therefore crucial to know the pressure loss across a stack for different configurations, as it is the element with the largest flow resistance in the airflow circuit of a kiln. In this respect the work in this section is of significance to the timber industry.

To determine the exact pressure loss across a stack, several methods are available. The first is to physically measure the pressure loss across a stack through which air is flowing as well as the air speeds at different operating points. A curve can then be fitted through the data to obtain an equation relating the pressure loss to air speed. Secondly, the flow can be solved numerically on a computer, but this is both time-consuming and expensive. The third is to model the flow characteristics mathematically with the additional benefit of revealing the critical parameters to be controlled for optimum performance. Both the first and last methods mentioned here are discussed and employed in this chapter.

Ideally, the boards in a stack should be of the same length as the wheel basis of a cart on which the timber is stacked. The timber logs cannot always be cut accordingly and it is then appropriate to cross-pile the boards in a stack as shown in Figure 6.2. The cross-pile method is used in most kilns around the world when necessary. A picture of such a stack is shown in Figure 6.3.

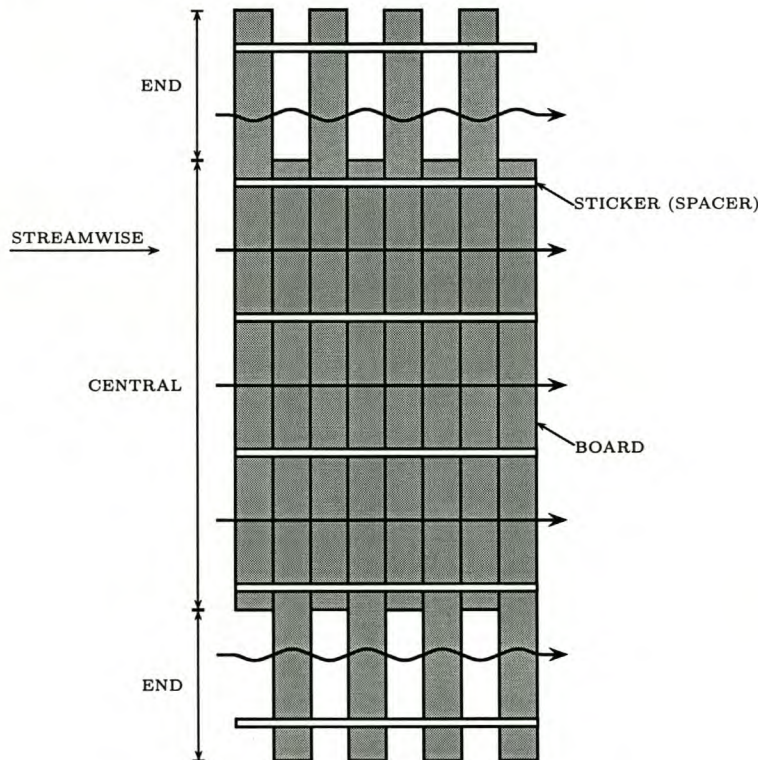


Figure 6.2: *Top view of a typical layer in a cross-piled stack showing stickers channelling the airflow in the streamwise direction. The board layers above and under the one shown is a mirror image of the displayed layer. Compare this with Figure 6.3 for clarity.*



Figure 6.3: A picture of a typical cross-piled timber stack to be dried in a kiln. Note the spacing of the stickers of which the ends are visible on the left. Picture taken at Mondi Timbers, Stellenbosch.

A pine timber stack is usually made up of layers as shown in Figure 6.2 and this method is used in virtually all South African kilns. From the figure it is clear that the stack can be divided into three parts concerning the flow characteristics. The first is the central area where the boards are against each other which creates flat, rectangular duct sections in the flow direction. The other two parts, one on each end, have a staggered layout and are treated as a porous medium with an anisotropic unidirectional fibrous microstructure. The RUC model of Chapter 4 is perfectly suited for the end parts and the central part is modelled as duct flow for which empirical solutions are readily available. An empirical solution given by Idelchik, 1986, which is applicable to the central part of a stack is also included for reference.

The measuring of velocities and pressure differences in a real kiln proved to be quite difficult because the quantities that have to be measured are both small and fluctuate considerably. This is most likely a direct result of turbulence generated by the fans or their the modal cycling from being in and out of phase. There are measures that can be employed to alleviate this, but it is not the only difficulty. The volume flow through a kiln cannot be regulated, as this is seldom a feature of the design. This results in only one operating point that can be measured. Another difficulty is that the cavity areas acting as plenum chambers before and after the airflow through the stack are not large enough to let the flow settle, resulting in local air velocities which are not constant in the streamwise direction. To overcome this challenge, two models of a stack, one resembling the centre and the other the end parts of a stack, were built and tested in a wind tunnel with steady and adjustable airflow. This allowed accurate flow data to be measured, providing a good reference to verify mathematical modelling accuracy.

6.1 Modelling of the Stack Centre

The ducts formed by the boards and stickers in the centre of a stack are shown in Figure 6.2 and the most important variable here is the duct hydraulic diameter defined as

$$d_h = \frac{4A}{\text{perimeter}}, \quad (6.1)$$

where A is the cross sectional area of the duct. The aspect ratio, AR , of these ducts is very low in practice with

$$AR = \frac{\text{duct height}}{\text{duct width}} < 0.1. \quad (6.2)$$

This is close to an infinitely wide duct of which the hydraulic diameter asymptotically approaches $d_h = 2 \times \text{duct height}$ (see Equation 6.1). This is a good approximation in most cases, but should be verified at higher aspect ratios.

The pressure loss of fully developed flow along a channel can be determined by using the Moody chart of Moody, 1944. The turbulent part of this chart is accurately approximated by the friction factor formula of Haaland, 1983, making mathematical representation possible. The dimensionless friction factor formula as determined by Haaland, 1983, represents the turbulent region on the Moody chart and is as follows:

$$f_D^{-\frac{1}{2}} = -1.8 \log_{10} \left(\frac{6.9}{Re_{Vd_h}} + \left(\frac{\varepsilon/d_h}{3.7} \right)^{1.11} \right), \quad (6.3)$$

where V is the average speed, for example $V_{L_{small}}$ in Figure 6.4. The surface roughness, ε , is estimated from measurements taken to be $2.5 - 5 \text{ mm}$ for non-planed boards (rough cut from logs) and about 0.2 mm for planed boards which are both within the possible ranges given by White, 1994. The head loss and pressure loss as defined by White, 1994, are given respectively by

$$h = \frac{f_D C V^2}{2g d_h}, \quad (6.4)$$

where C is the stack depth (distance in streamwise direction) and

$$\Delta P_{stack} = \rho g h + \Delta P_{SC} + \Delta P_{SE}. \quad (6.5)$$

Here the assumption is made that at the entrance the flow is from a larger to a smaller duct, called sudden contraction (SC). Although the walls of the large duct are only imaginary,

the assumption is valid because the flow is split in two along the centre of each board. The resulting flow pattern is that of sudden contraction and not simply flow from a large reservoir into an opening. The typical streamlines at a rectangular duct entrance are illustrated in Figure 6.4. At the exit of a duct there is a sudden expansion (SE) where a considerable amount of the kinetic flow energy is lost due to viscous dissipation (White, 1994).

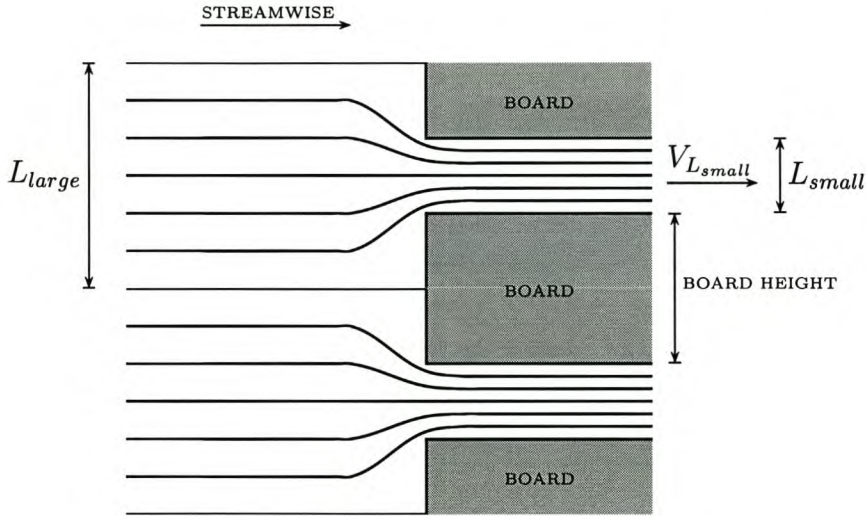


Figure 6.4: Illustration of streamlines in the region of sudden contraction between boards when the flow enters a stack.

The empirical pressure loss formula for sudden contraction for circular duct flow is given by White, 1994, as

$$\begin{aligned} \Delta P_{SC} &\approx 0.42 \left(1 - \frac{D_{small}^2}{D_{large}^2} \right) \frac{\rho V_{D_{small}}^2}{2} ; & 0 \leq \frac{D_{small}}{D_{large}} \leq 0.76 \\ \Delta P_{SC} &= \left(1 - \frac{D_{small}^2}{D_{large}^2} \right)^2 \frac{\rho V_{D_{small}}^2}{2} ; & \frac{D_{small}}{D_{large}} > 0.76, \end{aligned} \quad (6.6)$$

where $V_{D_{small}}$ is the average speed in the smaller tube and D is the pipe inner diameter. Equation 6.6 can be written in a more general form as

$$\begin{aligned} \Delta P_{SC} &\approx 0.42 \left(1 - \frac{A_{small}}{A_{large}} \right) \frac{\rho V_{L_{small}}^2}{2} ; & 0 \leq \frac{A_{small}}{A_{large}} \leq 0.578 \\ \Delta P_{SC} &= \left(1 - \frac{A_{small}}{A_{large}} \right)^2 \frac{\rho V_{L_{small}}^2}{2} ; & \frac{A_{small}}{A_{large}} > 0.578, \end{aligned} \quad (6.7)$$

where the square of the diameters were replaced by the cross-sectional areas, A , of the flow channel. In this form the sudden contraction formula is also applicable to shapes other than round. In similar fashion as above, the sudden expansion loss obtained from White, 1994, is

$$\Delta P_{SE} = \left(1 - \frac{A_{small}}{A_{large}}\right)^2 \frac{\rho V_{L_{small}}^2}{2}. \quad (6.8)$$

One might reason that all the kinetic energy would be lost upon exit, which implies that the air speed is stagnating in the open volume. However, this is not the case; hence the sudden expansion formula. This is the last tool necessary to determine a solution for the duct flow model of Equation 6.5. Lastly, the velocities q , $V_{L_{large}}$ and $V_{L_{small}}$ are simply related by

$$q = V_{L_{large}} = V_{L_{small}} \frac{A_{small}}{A_{large}}. \quad (6.9)$$

The equality in Equation 6.9 is possible because the speed, $V_{L_{large}}$, used in the larger channel of the sudden contraction model is exactly the same as the free stream speed, q , of the air approaching the stack.

Another model is the empirical one given by Idelchik, 1986, which is specifically developed to determine the pressure loss across a timber stack. The setup for which this solution is valid almost conforms to the central part of a stack as in Figure 6.2. However, the model of Idelchik, 1986, assumes the stack has horizontal spacings of about one board thickness between boards. The difference in permeability this would create in the stack model is considered to be minimal as the flow is not forced into the gaps between the boards as is the case when staggered. It should be noted that the gaps (down to 1 mm) significantly influence the evaporation from the timber, as described by Keey et al., 2000, due to the circulating flow in the gaps that periodically spills over into the boundary layer of the channel flow between the boards. The expression given by Idelchik, 1986, is in the current notation as follows:

$$\Delta P_{stack} = \frac{\rho q^2 \lambda C}{2d_h \epsilon^2}, \quad \text{where} \quad \begin{aligned} \lambda &= \frac{3.2}{Re_{qd_h}^{0.375}} ; & 4 \times 10^2 < Re_{qd_h} < 10^4 \\ \lambda &= 0.1 ; & Re_{qd_h} \geq 10^4. \end{aligned} \quad (6.10)$$

In this case q refers to the speed approaching the stack centre and d_h is the hydraulic diameter of the vertical spacing between the boards. To make comparisons possible with an experimental model of a stack centre, the dimensions of the experimental model are modified by inserting spacing gaps of one board thickness between the boards before calculating the relevant values necessary for the empirical model of, Idelchik, 1986. This is done in Section 6.3, where the stack depth, C , and porosity, ϵ , include the spacing gaps inserted between the boards.

6.2 Modelling of the Stack Ends

In the end parts of a stack, the boards are in a staggered configuration, which is a direct result of the stacking method, as discussed previously. The flow through these ends are analyzed with the RUC model described in Chapter 4. The results obtained are fairly accurate when compared to the experimental data, because the rectangular shape of the timber boards are similar to those used in the RUC model and are also well staggered.

The general layout of the timber boards at the end of a stack is shown in Figure 6.5 with the smallest periodic volume also indicated. The starting point in the analysis is to obtain applicable values for C_D to use in Equations 4.32 to 4.34. White, 1994, published data as given in Table 6.1 of the drag coefficient for a range of rectangular cylinders of which the aspect ratio varies.

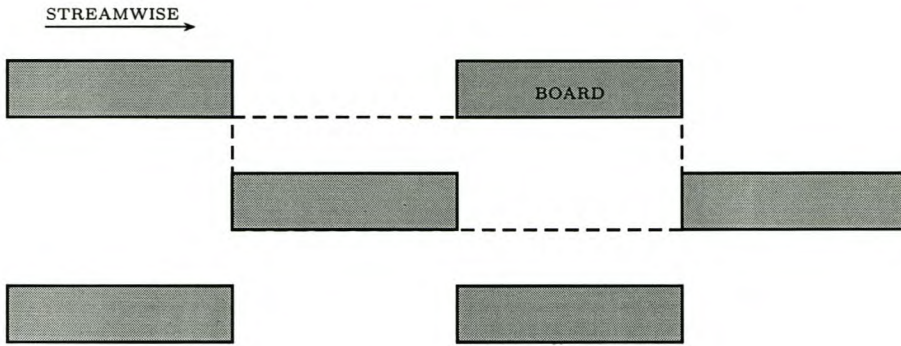
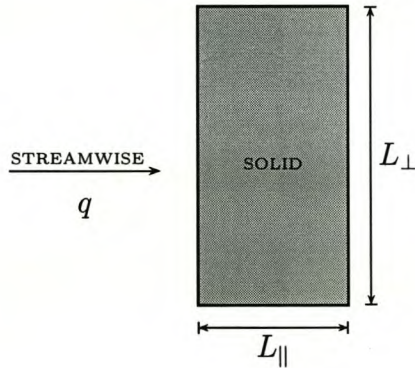


Figure 6.5: A view of a section through the stack end perpendicular to the streamwise direction with the area inside the dashed line, showing the size of the smallest periodic volume.

Table 6.1: C_D for 2-D rectangular bodies at $Re_{qL_{\perp}} \geq 10^4$ from White, 1994.

L_{\parallel}/L_{\perp}	C_D
0.1	1.9
0.4	2.3
0.7	2.7
1.2	2.1
2.0	1.8
2.5	1.4
3.0	1.3
6.0	0.9



A curve fit through the data of White, 1994, as given in Table 6.1, results in the following:

$$C_D = \left(c_5 + c_6 \left(\frac{d_{s\parallel}}{d_{s\perp}} \right) + c_7 \left(\frac{d_{s\parallel}}{d_{s\perp}} \right)^2 \right)^{-1}, \quad \text{where} \quad \begin{aligned} c_5 &= 0.2377 \\ c_6 &= 0.1979 \\ c_7 &= -0.008485. \end{aligned} \quad (6.11)$$

All the other variables necessary to use in the RUC model as given in Equations 4.32 to 4.34 can be obtained directly from the geometry of the test model or from the fluid properties themselves.

6.3 Experimental Analysis of the Stack Centre

The wind tunnel used to obtain the experimental flow results in this section is located in a laboratory of the Department of Mechanical Engineering at the University of Stellenbosch. It was built specifically to perform flow tests on heat exchangers up to about $1m^2$ with a maximum volume flow in the region of $1m^3/s$, depending on the model resistance. The experimental stack model of the stack centre was designed to fit snugly in the wind tunnel to ensure that all the air is forced through it. This necessitates the model dimensions to conform to the tunnel dimensions. Figure 6.6 shows the basic experimental setup, representing the centre of a stack, with the tunnel inlet towards the front. The position of the model relatively close to the inlet ensures a uniform approach speed of the air. The timber boards used in the model are linearly scaled versions of a popular timber board size with dimensions $120 \times 40 \text{ mm}$ if wet and $114 \times 38 \text{ mm}$ when dry. The dimensions of this stack model is given in Table 6.2.

Table 6.2: *Dimensional values of experimental stack resembling the centre of a real stack.*

Description	Value [mm]	Variable
Stack width	468	—
Stack height	500	—
Stack depth	455	C
Board width	65	—
Board height (thickness)	20.6	—
Sticker width	20	—
Sticker height	12.6	L_{small}
Distance between stickers	428	—

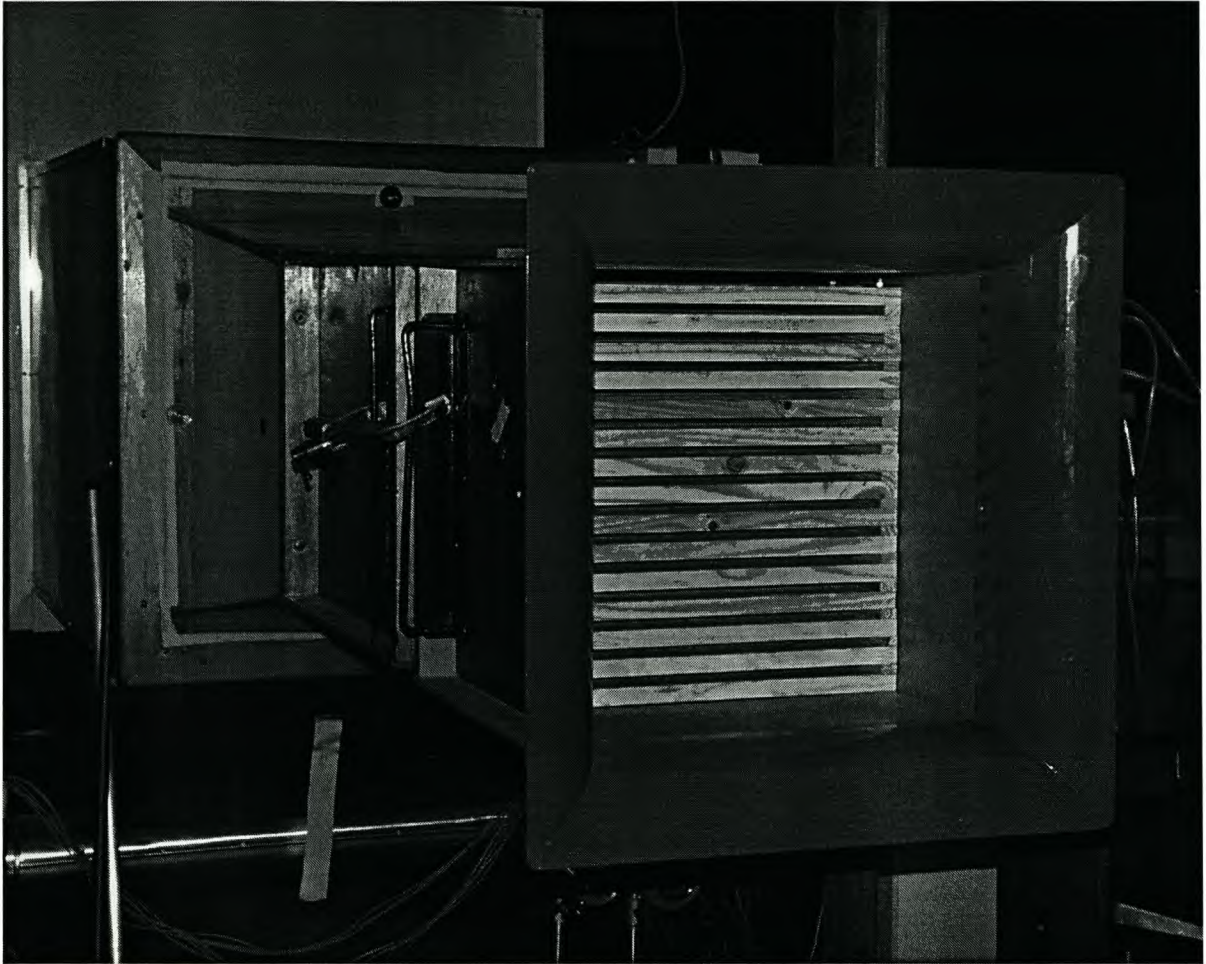


Figure 6.6: *Picture of an experimental stack in a wind-tunnel. Model of central part seen from tunnel inlet.*

The equipment used for measurement was a set of Betz manometers to measure the pressure difference across the stack, as well as a set of standard Bernoulli obstruction flow meters (ISO elliptic long radius nozzles) fitted in the tunnel. The readings from the mouth pieces, together with the ambient air properties, were used to calculate the volume airflow from which the air speed through the stack can be determined. The measured data was verified by first incrementally increasing and then decreasing the airflow through the test range to check if similar results were obtained. Table 6.3 lists the air properties which were present during the experiment.

Table 6.3: *Air properties present during experiment.*

Property	Value		Variable
Temperature	20	[°C]	—
Density ¹	1.2	[kg/m ³]	ρ
Humidity	60	[%]	—
Viscosity ¹	1.8×10^{-5}	[N · s/m ²]	μ

The results obtained from the experiment in the wind tunnel are given in Table 6.4, where the volume flow, Q , is the total flow through the stack model. The test range of the wind tunnel was limited by its flow capacity and therefore the whole Darcy and Reynolds flow ranges could not be covered with a single experimental setup. The data obtained, however, is adequate for comparison, as it covers the range of operating points for timber-drying kilns.

Table 6.4: *Experimental data obtained from the stack centre model in the wind tunnel.*

Airflow, Q [m ³ /s]	Δp_{stack} [Pa]
0.07413	1.3
0.10950	2.8
0.16628	5
0.24784	10
0.43340	26
0.63064	53
0.85362	95

The airflow values given in Table 6.4 can be converted to the air speed approaching the stack with

$$\begin{aligned}
 q &= Q \times \text{frontal area of the stack} \\
 &= Q \times \text{distance between stickers} \times \text{stack height}.
 \end{aligned}
 \tag{6.12}$$

¹Values determined from standard psychometric tables

6.4 Experimental Analysis of the Stack Ends

The model for the stack ends used for this analysis was tested in the same wind tunnel as the model of the stack centre. A picture of the actual model is shown in Figure 6.7, from which it is evident that the flow pattern will be close to that of the RUC model in Chapter 4. The timber boards used are also the same size as in the previous experiment. The dimensioning of this stack model is given in Table 6.5 and Table 6.6 lists the air properties which were present during the experiment.

Table 6.5: *Dimensional values as used in the RUC of the experimental stack to model the staggered ends of a real stack.*

Description	Value [mm]	Variable
Stack width	468	—
Stack height	485	—
Stack depth	455	C
Board width	65	$d_{s\parallel}$
Board height (thickness)	20.6	$d_{s\perp}$
Sticker width	20	—
Sticker height	12.6	$d_{p\perp}$
Distance between stickers	428	—

Table 6.6: *Air properties present during experiments.*

Property	Value	Variable
Temperature	20 [°C]	—
Density ²	1.2 [kg/m ³]	ρ
Humidity	60 [%]	—
Viscosity ²	1.8×10^{-5} [N · s/m ²]	μ

²Values determined from standard psychometric tables

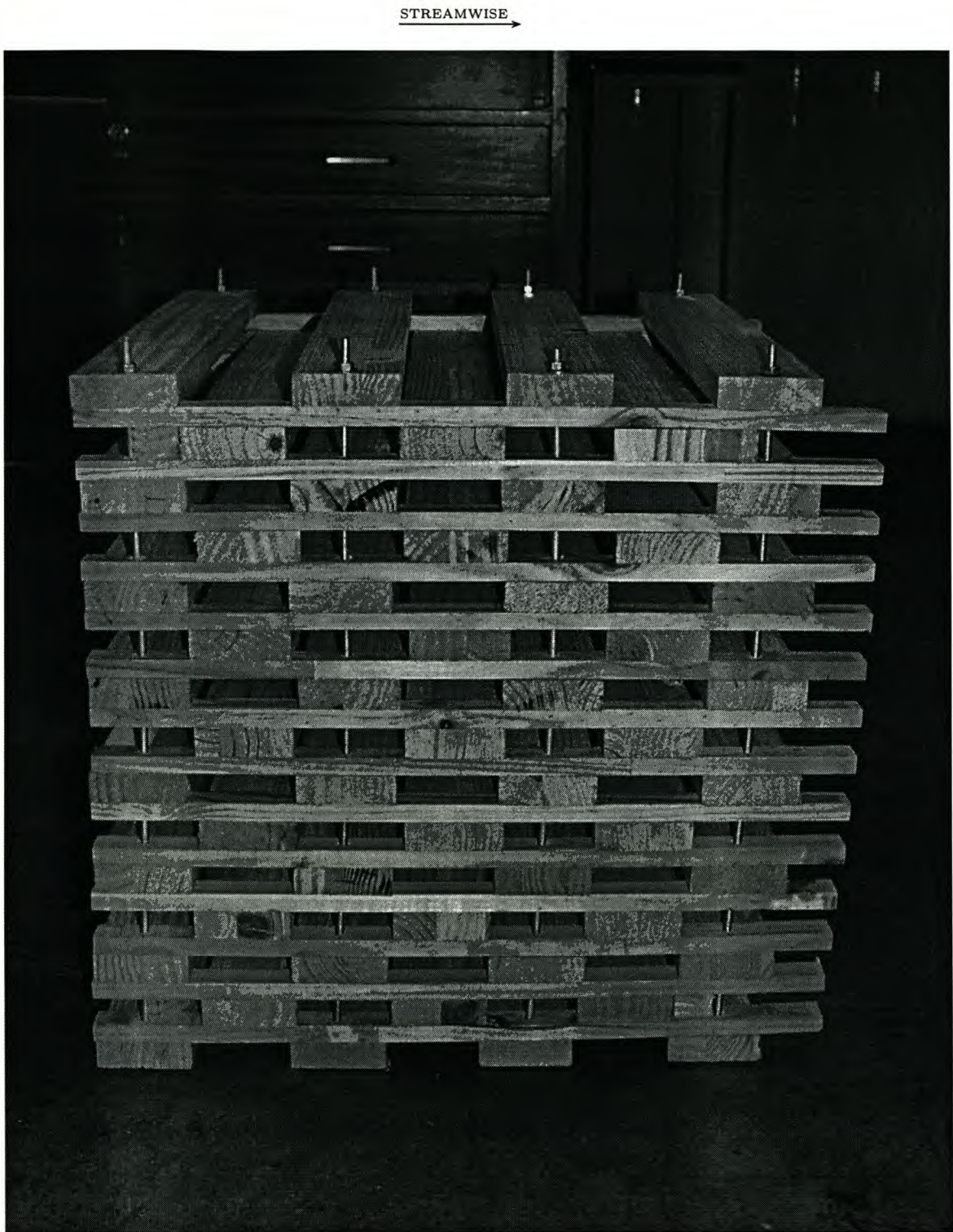


Figure 6.7: *Test model of stack end with the streamwise direction from left to right.*

Results obtained from the wind tunnel experiments are given in Table 6.7. The difference between this model and the previous one is that the horizontal gaps between the board layers were created by taking out every second board according to the lay-up shown in Figure 6.2.

Table 6.7: *Experimental data obtained from the model of a stack end in the wind tunnel.*

Airflow [m^3/s]	Δp_{stack} [Pa]
0.07422	2.5
0.11036	6
0.15685	10
0.23256	23
0.37496	55
0.56138	126
0.81999	271.5
$\epsilon = 0.69$	

6.5 Comparison of Results

In this section, the three RUC models are applied to timber stacks and evaluated against the experimental results. All the data can be combined on one plot in terms of the average speed between the boards and the total pressure loss across the experimental stack models.

Figure 6.8 illustrates the difference between the three RUC models of 4.32 to 4.34 with the values used in the RUC models given in Table 6.8. The experimental data of the model for the stack ends are also given for comparison purposes. Of the three solutions from the RUC theory, only the RUC model of Equation 4.33 closely follows the experimental data of the experimental model. The other two have similar solutions but are not near to the experimental data. The value for C_D in this case is 1.29 and $\beta = 0.19$, which clearly shows that replacing C_D with the factor β^2 or βC_D would give a totally different result. If the boards were to have a more square shape, β would increase considerably resulting in better results obtained from the three RUC models. This indicates that the use of β is not well

suitable for anisotropic porous media, and that Equations 4.25 or 4.33 are more suitable for this particular application.

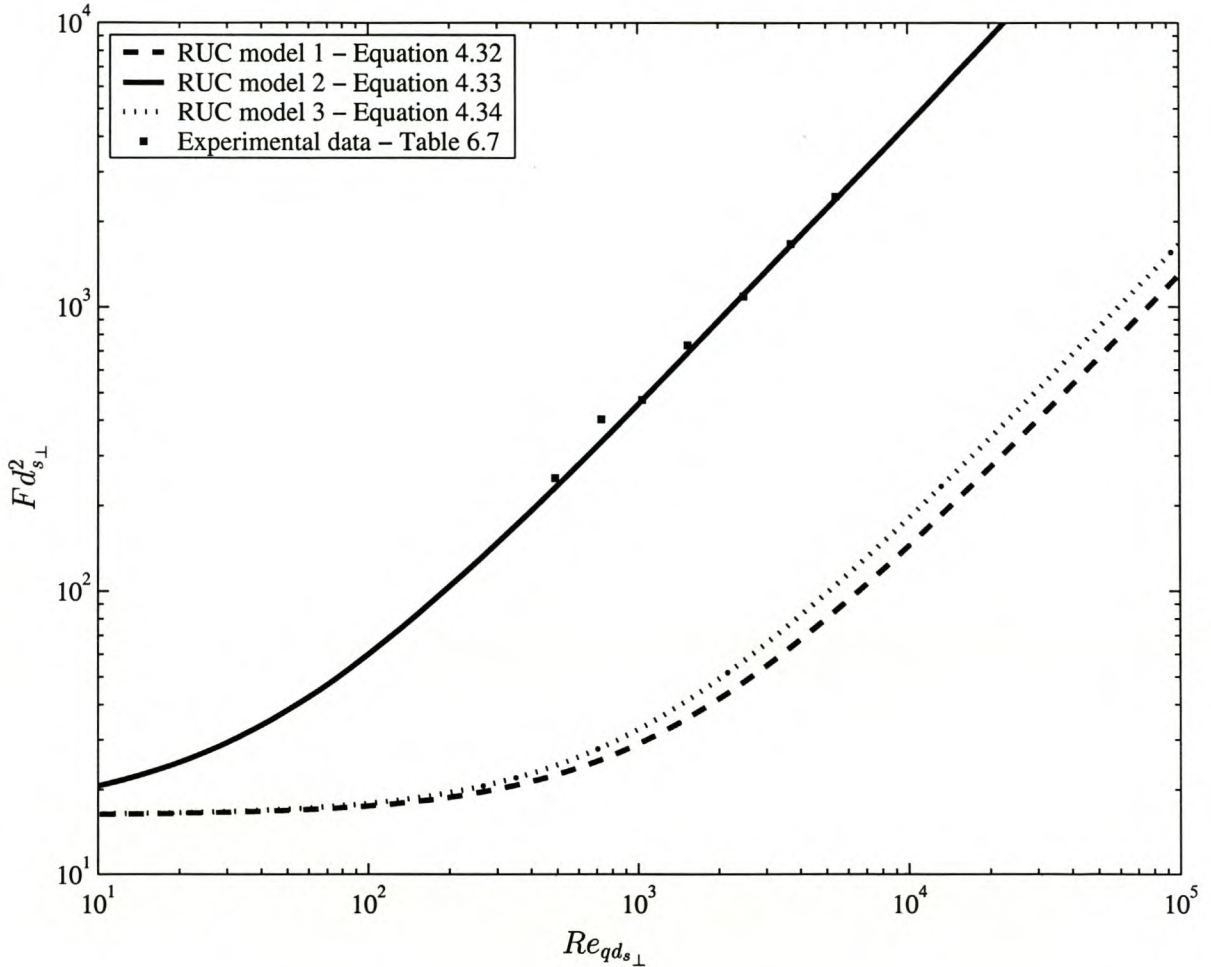


Figure 6.8: *The comparison of the three mathematical solutions in Chapter 4 and the experimental data from the stack end model.*

It is quite useful to make a plot as in Figure 6.9 to compare the flow through the different specific stack configurations. This not only gives insight to the actual gradient of the flow resistance curve of a stack, but also to the actual average flow velocities that are present in a stack. The values used to plot the curves for the duct flow and empirical model by Idelchik, 1986, are given in Table 6.9.

Table 6.8: Values used to produce results for the RUC solution plotted in Figure 6.8.

Variable	Value	Variable	Value
d_{\perp}	0.0332 [m]	ϵ	0.69
d_{\parallel}	0.130 [m]	χ	1.82
$d_{s\perp}$	0.0206 [m]	β	0.19
$d_{s\parallel}$	0.065 [m]	C_D	1.29
U_o/z	0.0044 [m ²]		

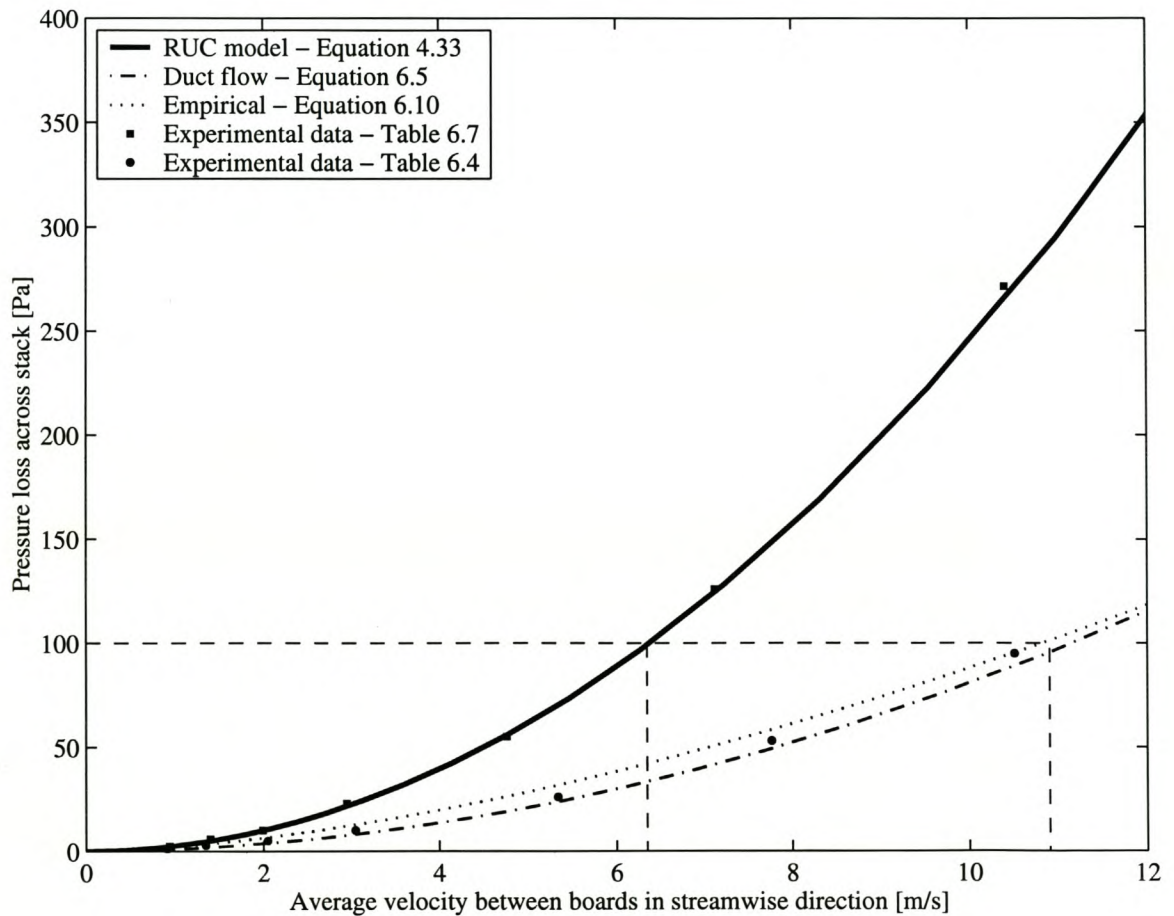


Figure 6.9: Pressure loss across the experimental stacks as tested in the wind tunnel compared with mathematical models.

Table 6.9: Values used for the stack centre models of duct flow and Idelchik, 1986, which are plotted in Figure 6.9. Note the difference between ε (surface roughness) and ϵ (porosity).

Variable	Value
Duct flow model	
ε	0.0002 []
d_h	0.025 [m]
C	0.455 [m]
g	9.81 [m/s^2]
A_{small}	0.0054 [m^2]
A_{large}	0.0142 [m^2]
ρ	1.2 [kg/M^3]
Idelchik, 1986, model	
ϵ	0.53 []
d_h	0.025 [m]
C	0.60 [m]

The actual drying rate of the timber boards do not only depend on the air speed and vertical gradient on the upper and lower board surfaces, but also on the humidity and air temperature. Frequent reversal of the air direction through the kiln averages the streamwise temperature and humidity gradients out across a stack. Thus, the only manner to get the drying rate even throughout the stack is to have the same speed gradient on the upper and lower surfaces of each board throughout a stack.

When collecting data in real timber kilns³, it was noticed that the pressure difference across a stack is the same for the centre and end parts during kiln operation, but the velocities between the boards were different. The most probable reason for the constant pressure difference is that the relatively slow moving flow is free to settle in the plenum chamber volumes before entering and after exiting a stack. The geometrical aspects of the macroscopic flow in the plenum areas are described in Nijdam and Keey, 1999, and Nijdam and Keey,

³Timber kilns at Mondi Timbers, Stellenbosch

2000. The result of this phenomenon is that the pressure difference across a stack is constant and the speed differences are only dependent on the local streamwise permeability of the stack itself. Figure 6.9 can thus be used in the following manner with a fixed pressure difference assumed across a stack, say $dP = 100 \text{ Pa}$. The average flow velocities between the boards of each stack section can then be read off using the respective curves.

For convenience, the simple analysis described above is illustrated in Figure 6.9 with dashed lines. If the plane Poiseuille flow model is assumed to be valid for the flow between the boards in both experimental models, the speed gradients can be obtained for a specific pressure difference across a whole stack. The results for the case where the pressure difference across both the experimental stacks is 100 Pa are listed in Table 6.10.

Table 6.10: *Example of how Figure 6.9 can be interpreted.*

	Stack centre	Stack end
dP_{stack}	100 [Pa]	100 [Pa]
$V_{avg, \text{ between boards}}$	10.9 [m/s]	6.35 [m/s]
$\left(\frac{dv}{dy}\right)_{fs }$	5190 [s^{-1}]	1148 [s^{-1}]

In Table 6.10 the speed gradient, $\left(\frac{dv}{dy}\right)_{fs||}$, is calculated by using Equation B.4 of the Poiseuille flow model. These values show that the velocity gradient at the streamwise surfaces of the boards is more than 4.5 times higher for the stack centre than the staggered ends. This negative effect this could have on the drying of the boards has already been mentioned. Fortunately, one phenomenon that counters this to some extent is the drying properties of a timber board itself. The board ends dry more quickly than the board centre due to the open pores at the board tips which freely allow for the transportation of moisture between the atmosphere and the inside of the boards. This results in a stacking method that works, but also leaves some room for improvement.

One final comment: The air properties inside a real kiln might range from ambient temperature and relative humidity up to 100°C with a relative humidity of 100%. The appropriate air properties should always be used for any analysis as they can have a considerable influence on results obtained.

Chapter 7

Conclusions and Recommendations

The first part of this study is devoted to the background of the mathematical modelling of porous media. Secondly, the basics of the Representative Elementary Volume (REV) theory are given which forms the basis of porous media modelling. Thereafter, the fluid transport equations are applied to REV's by means of Representative Unit Cells (RUC) which model the flow and geometry to be in a rectangular fashion. The theory presented is then applied to two industrially related problems that have the characteristics of flow through two-dimensional porous media. The first application is on cross-flow through tube banks, where both staggered and square array cases are investigated. Flow through a stack in a timber-drying kiln is the second application that is modelled and the most important aspects of timber-drying are also discussed.

The REV theory that is presented in this thesis is applicable to both two- and three-dimensional porous media. This theory forms the basis of porous media modelling upon which different secondary models can be built to specifically meet the requirements of both the porous medium and flow characteristics to be modelled.

The RUC model, which is built on the REV theory, is given in two-dimensional form to be directly applicable to the two-dimensional applications investigated. The RUC model that is presented (from Diedericks, 1999) is applicable to two-dimensional porous media, which may have anisotropic characteristics. Both the momentum transport and continuity equations

are employed in this model to arrive at a solution for each of the Darcy and Forchheimer flow regimes. The combination of the two flow regime solutions is done with the asymptote matching technique of Churchill and Usagi, 1972, which produces a result that is applicable to the whole range of low and intermediate Reynolds numbers.

Cross-flow in tube banks is the first industrial application in this work to which the RUC model is applied. This is done for both staggered and square cases and the results are compared with the data of Zukauskas and Ulinskas, 1983. The results obtained from the RUC model give a good indication of the pressure losses that can be expected through a tube bank at different flow rates. The RUC model is found to be more suitable for staggered banks because the flow characteristics are similar, a fact which is also reflected in the comparison of results.

The second industrial application of the RUC theory is to stacks of timber-drying kilns. A typical stack possesses two types of flow regions. The ends parts are modelled with the anisotropic RUC theory and the central part with duct flow. Both these regions are accurately modelled when the results are compared to the experimental data obtained from the models tested in a wind tunnel. This makes it possible to model the flow characteristics completely through a timber-drying kiln, providing a tool to optimize kiln design further.

The application of the two-dimensional anisotropic RUC model can be extended to a wide range of applications, e.g. flow through skyscraper buildings and certain fibrous filters. The model could possibly be modified to make it more useful and accurate as engineering tool for design and flow analysis of phenomena with a prismatic structure. This could be achieved by further practical applications of the model, as was done in this thesis, to other scenarios. Ways to further refine the model may surface during such studies and the practical of working with the model will give insight towards its applicability and limitations.

Application of Computational Fluid Dynamics software, for example CFX 5.4.1, can give very accurate insight into the actual flow patterns inside a porous medium. It might be possible to modify the RUC model from this source of information to more accurately model the flow characteristics. The RUC model, for example, assumes plane Poiseuille flow between parallel plates at the lower flow limit as $Re \rightarrow 0$, where another model could be more

appropriate to use as the flow channels are very short and the flow does not have time to become fully developed. It would also be very useful to investigate at which Reynolds number ranges the interstitial flow of a given porous medium type becomes turbulent.

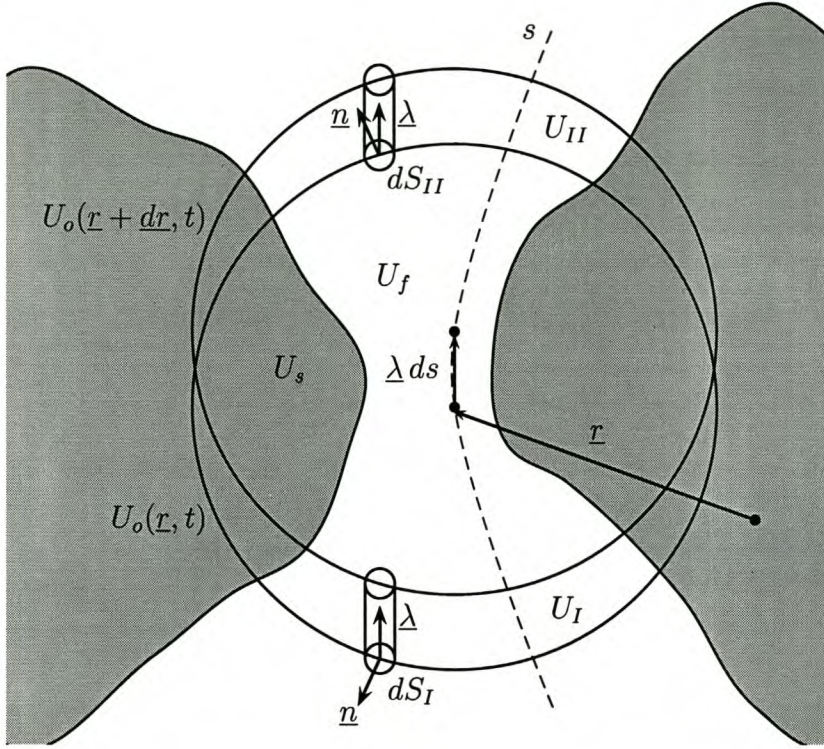
Appendix A

Slattery's Averaging Theorem

Spacial averaging in a porous medium can be done with the application of Slattery's averaging theorem. This theorem enables one to express, for a tensorial function, the gradient of an average as the average of the gradient of a function as done in Section 2.2. Several routes can be taken to arrive at the averaging theorem. Slattery, 1967, developed this theorem when studying viscoelastic flow through porous media. This theorem is recapped and fully discussed in the recent work of Slattery, 1999. Whitaker, 1967, also developed the theorem independently at the same time as Slattery in 1967. The method that Whitaker, 1985, used to arrive at the above result is summarized here.

Consider two REV's of the same size with centroids at \underline{r} and $\underline{r} + \underline{dr}$ such that $\underline{dr} = \underline{\lambda} ds$, where $\underline{\lambda}$ is a unit vector tangent to the arbitrary curve, s . Both these REV's are considered at the same time and are shown in Figure A.1. It is convenient to start at the directional derivative and by also using the definition of the derivative, we can write:

$$\begin{aligned}
 \mathcal{I} &\equiv \underline{\lambda} \cdot \nabla \iiint_{U_f(s,t)} \psi(\underline{r}, t) dU \\
 &= \frac{d}{ds} \iiint_{U_f(s,t)} \psi(\underline{r}, t) dU \\
 &= \lim_{\Delta s \rightarrow 0} \frac{1}{\Delta s} \left[\iiint_{U_f(s+\Delta s,t)} \psi(\underline{r}, t) dU - \iiint_{U_f(s,t)} \psi(\underline{r}, t) dU \right], \tag{A.1}
 \end{aligned}$$

Figure A.1: Translation of a REV along an arbitrary curve s .

It is evident from Figure A.1 that the overlapping regions of the last two integrals in Equation A.1 cancel out which results in

$$\mathcal{I} = \lim_{\Delta s \rightarrow 0} \frac{1}{\Delta s} \left[\iiint_{U_{II}(s+\Delta s, t)} \psi(\underline{r}, t) dU_{II} - \iiint_{U_I(s, t)} \psi(\underline{r}, t) dU_I \right]. \quad (\text{A.2})$$

The volume integrals, U_I and U_{II} , can be transformed to surface integrals by substitution of the two equalities:

$$dU_I = -\underline{\lambda} \cdot \underline{n} \Delta s dS_I \quad (\text{A.3})$$

$$dU_{II} = \underline{\lambda} \cdot \underline{n} \Delta s dS_{II}, \quad (\text{A.4})$$

resulting in

$$\mathcal{I} = \lim_{\Delta s \rightarrow 0} \frac{1}{\Delta s} \left[\iint_{S_{II}} \underline{\lambda} \cdot \underline{n} \psi dS_{II} + \iint_{S_I} \underline{\lambda} \cdot \underline{n} \psi dS_I + \mathcal{O}(\psi l (\Delta s)^2) \right]. \quad (\text{A.5})$$

The term $\mathcal{O}(\psi l(\Delta s)^2)$ is the order of the error created when the volume integrals are transformed. The constants, $\underline{\lambda}$ and Δs , can be moved across the integrals allowing Equation A.5 to be written as

$$\mathcal{I} = \lim_{\Delta s \rightarrow 0} \left[\underline{\lambda} \cdot \iint_{S_{II}} \underline{n}\psi dS_{II} + \underline{\lambda} \cdot \iint_{S_I} \underline{n}\psi dS_I + \Delta s \mathcal{O}(\psi l) \right]. \quad (\text{A.6})$$

The last term becomes null in the limit where $\Delta s \rightarrow 0$, yielding

$$\mathcal{I} = \underline{\nabla} \cdot \iint_{S_{ff}} \underline{n}\psi dS. \quad (\text{A.7})$$

When Equation A.7 is substituted into Equation A.1, Slattery's averaging theorem is obtained, which is as follow:

$$\underline{\nabla} \iiint_{U_f} dU = \iint_{S_{ff}} \underline{n}\psi dS. \quad (\text{A.8})$$

Appendix B

Plane Poiseuille Flow

Plane Poiseuille flow is defined as the fully developed laminar viscous flow between two parallel plates with infinite dimensions. This flow model is available in many fluid mechanical publications, e.g. White, 1994. The velocity profile is determined by starting with the Navier-Stokes Equation using the dimensions defined in Figure B.1.

Solving the 1D Navier Stokes-equation, obtained from Equation 3.14, and applying the no-slip boundary conditions at the plates, produces the result:

$$v(y) = -\frac{y}{2\mu} \left(\frac{dP}{dx} \right) (L - y), \quad (\text{B.1})$$

where $\frac{dP}{dx}$ is the pressure gradient (the conservation of mass, $\frac{\partial v}{\partial x} = 0$, implies that $v = v(y)$). The average speed is now calculated by integration over the distance between the plates as follows:

$$V = -\frac{dP}{dx} \frac{1}{L} \int_0^L \left(-\frac{yL}{2\mu} + \frac{y^2}{2\mu} \right) dy \quad (\text{B.2})$$

thus,

$$\frac{dP}{dx} = -\frac{12\mu V}{L^2}, \quad (\text{B.3})$$

where V is the average speed between the plates.

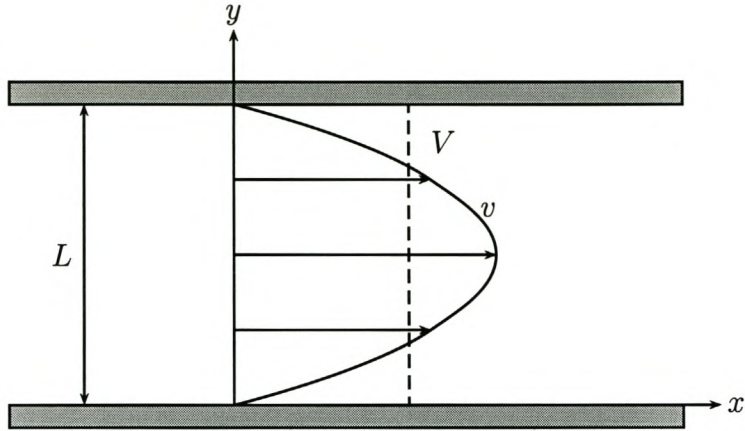


Figure B.1: *Plane Poiseuille flow between stationary parallel plates.*

The wall shear stress, τ_w , can now be expressed in terms of the averaged speed as:

$$\begin{aligned}
 \tau_{w,y=0} &= \mu \left(\frac{dv}{dy} \right)_{y=0} \\
 &= \mu \left(-\frac{L}{2\mu} \frac{dP}{dx} + \frac{y}{\mu} \frac{dP}{dx} \right)_{y=0} \\
 &= \frac{6\mu V}{L}.
 \end{aligned} \tag{B.4}$$

This result is used to model the flow inside the RUC for the Darcy flow range in Chapter 4.

Bibliography

Bear, J., *Dynamics of Fluids in Porous Media*, Elsevier, New York, 1972.

Bear, J. and Bachmat, Y., *Introduction to Modelling of Transport Phenomena in Porous Media*, Kluwer Academic Publishers, The Netherlands, 1991.

Bear, J. and Buchlin, J-M., *Modelling and Applications of Transport Phenomena in Porous Media*, Kluwer Academic Publishers, The Netherlands, 1991.

Bergelin¹, O.P., Colburn, A.P. and Hull, H.L., *Heat Transfer and Pressure Drop During Viscous Flow Across Unbaffled Tube Banks*, University of Delaware, Newark, Bulletin No.2, 1950.

Bird, R.B., Stewart, W.E. and Lightfoot, E.N., *Transport Phenomena*, John Wiley, New York, 1960.

Carman, P.C., Fluid Flow through Granular Beds, *Transactions of the Institution of Chemical Engineers*, Volume 15, 1937, pp. 150-166.

Churchill, S.W. and Usagi R., A General Expression for the Correlation of Rates of Transfer and Other Phenomena, *American Institute of Chemical Engineering Journal*, Volume 18, No. 6, pp. 1123-1128, 1972.

Darcy², H.P.G., *Les Fontaines Publiques de la Ville de Dijon*, Victor Dalmont, Paris, 1856.

¹Reference not read. Referred to by Zukauskas and Ulinskas, 1983.

²Reference not read. Referred to by Carman, 1937.

- Diedericks, G.P.J., *Pore-scale Modelling of Transport Phenomena in Homogeneous Porous Media*, PhD Thesis, University of Stellenbosch, South Africa, 1999.
- Diedericks, G.P.J. and Du Plessis, J.P., On Tortuosity and Anisotropy Tensors for Porous Media, *Transport in Porous Media*, Volume 20, No. 3, pp. 265-279, 1995.
- Dullien, F.A.L., *Porous Media: Fluid Transport and Pore Structure*, Academic Press, 1979.
- Du Plessis, J.P., Saturated flow through a Two-dimensional Porous Medium, *Transport in Porous Media*, Volume 6, pp. 207-221, 1991.
- Du Plessis, J.P., Fluid Transport in Porous Media, *Advances in Fluid Mechanics*, Volume 13, Computational Mechanics Publications, pp. 61-104, 1997.
- Du Plessis, J.P. and Masliyah, J.H., Mathematical Modelling of Flow Through Consolidated Porous Media, *Transport in Porous Media*, Volume 3, pp. 145-161, 1988.
- Du Plessis, J.P. and Van der Westhuizen, J., Laminar Crossflow Through Prismatic Porous Domains, *R&D Journal*, Volume 9, No. 2, 1993.
- Ergun, S., Fluid Flow Through Packed Columns, *Chemical Engineering Progress*, Volume 48, No. 2, pp. 89-94, 1952.
- Forchheimer³, P., Wasserbewegung durch Boden, *Zeitung Ver. Deutsch. Ing.*, Volume 45, 1937.
- Gebart, B.R., Permeability of Unidirectional Reinforcements for RTM, *Journal of Composite Materials*, Volume 26, pp. 1100-1133, 1992.
- Howells, I.D., Drag on Fixed Beds of Fibres in Slow Flow, *Journal of Fluid Mechanics*, Volume 355, pp. 163-192, 1998.
- Haaland, S.E., Simple and Explicit Formulas for the Friction Factor in Turbulent Pipe Flow, *Journal of Fluids Engineering*, March 1983, pp. 89-90.

³Reference not read. Referred to by Carman, 1937.

Idelchik, I.E., *Handbook of Hydraulic Resistance: Second Edition, Revised and Augmented*, Hemisphere Publishing Corporation, 1986.

Jackson, G.W. and James, D.F., The Permeability of Fibrous Porous Media, *Canadian Journal of Chemical Engineering*, Volume 64, June 1986.

Key, R.B., Langrish, T.A.G. and Walker, J.C.F., *Kiln-Drying of Lumber*, Springer Series in Wood Science, Springer, 2000.

Koehler, A. and Thelen, R., *The Kiln Drying of Lumber*, McGraw-Hill Book Company, New York, 1926.

Kolodziej, J.A., Filtration Resistance of a System of Parallel Cylinders at a Transverse Creeping Flow, *Mechanika Teoretyczna i Stosowana*, Volume 24, No. 4, 1986.

Nijdam, J.J. and Key R.B., Airflow Behavior in Timber (Lumber) Kilns, *Drying Technology*, Volume 17, pp. 1511-1522, 1999.

Nijdam, J.J. and Key R.B., Influence of Kiln Geometry on Flow Maldistribution Across Timber Stacks in Kilns, *Drying Technology*, Volume 18, pp. 1865-1877, 2000.

Moody⁴, L. F., Friction Factors for Pipe Flow, *Transaction of the ASME*, Volume 66, pp. 671-684, 1944.

Quintard, M. and Whitaker, S., Transport in ordered and disordered porous media I: The cellular average and the Use of Weighting Functions, *Transport in Porous Media*, Volume 14, pp. 163-177, 1994.

Reynolds⁵, O., *Papers on Mechanical and Physical Subjects*, Cambridge University Press, 1900.

⁴Reference not read. Referred to by White, 1994

⁵Reference not read. Referred to by Ergun, 1952.

- Sadiq, T.A.K., Advani, S.G. and Parnas, R.S., Experimental Investigation of Transverse Flow Through Aligned Cylinders, *International Journal of Multiphase Flow*, Volume 21, No.5, pp. 755-774, 1995.
- Sangani, A.S. and Acrivos, A., Slow Flow Past Periodic Arrays of Cylinders with Application to Heat Transfer, *International Journal of Multiphase Flow*, Volume 8, No. 3, pp. 193-206, 1982.
- Shah, R.K. and London, A.L., *Laminar Flow Forced Convection in Ducts*, Academic, New York, 1979.
- Slattery, J.C., Flow of Viscoelastic Fluids Through Porous Media, *American Institute of Chemical Engineering Journal*, Volume 13, pp. 1066-1071, 1967.
- Slattery, J.C., *Advanced Transport Phenomena*, Cambridge University Press, 1999.
- Travkin, V.S. and Catton, I., Transport Phenomena in Heterogeneous Media Based on Volume Averaging Theory, *Advances in Heat Transfer*, Volume 34, pp. 1-133, 2001.
- Van der Westhuizen, J. and Du Plessis, J.P., Quantification of Unidirectional Fiber Bed Permeability, *Journal of Composite Materials*, Volume 28, No. 7, 1994.
- Whitaker, S., A Simple Geometrical Derivation of The Spatial Averaging Theorem, *Chemical Engineering Education*, Volume 19, pp. 18-21 and 50-52, 1985.
- Whitaker, S., Diffusion and Dispersion in Porous Media, *American Institute of Chemical Engineering Journal*, Volume 13, pp. 420-427, 1967.
- White, F.M., *Fluid Mechanics: Third Edition*, McGraw-Hill, Inc, 1994.
- Zukauskas, A. and Ulinskas, R., Banks of Plain and Finned Tubes, *Heat Exchanger Design Handbook*, Section 2.2.4-1, 1983.
- Zukauskas, A., Heat Transfer from Tubes in Crossflow, *Advances in Heat Transfer*, Volume 18, pp. 87-159, 1987.